9-15-2022

Difference in seasonal peak timing of soybean far-red SIF and GPP explained by canopy structure and chlorophyll content

Genghong Wu
University of Illinois Urbana-Champaign

Chongya Jiang
University of Illinois Urbana-Champaign

Hyungsuk Kimm
University of Illinois Urbana-Champaign

Sheng Wang
University of Illinois Urbana-Champaign

Carl Bernacchi
USDA ARS

See next page for additional authors

Remote Sensing of Environment 279 (2022) 113104

Contents lists available at ScienceDirect

Remote Sensing of Environment

journal homepage: www.elsevier.com/locate/rse

Difference in seasonal peak timing of soybean far-red SIF and GPP explained by canopy structure and chlorophyll content

Genghong Wu [a,b], Chongya Jiang [a,b,*], Hyungsuk Kimm [a,b], Sheng Wang [a,b], Carl Bernacchi [c,d], Caitlin E. Moore [c,e,f], Andy Suyker [g], Xi Yang [h], Troy Magney [i], Christian Frankenberg [j,k], Youngryel Ryu [l,m], Benjamin Dechant [l], Kaiyu Guan [a,b,n,*]

[a] Agroecosystem Sustainability Center, Institute for Sustainability, Energy, and Environment, University of Illinois at Urbana-Champaign, Urbana, IL, USA
[b] Department of Natural Resources and Environmental Sciences, College of Agricultural, Consumer and Environmental Sciences, University of Illinois at Urbana-Champaign, Urbana, IL, USA
[c] Department of Plant Biology, University of Illinois at Urbana-Champaign, Urbana, IL, USA
[d] USDA-ARS, Global Change and Photosynthesis Research Unit, Urbana, IL, USA
[e] Institute for Sustainability, Energy and Environment, University of Illinois at Urbana-Champaign, Urbana, IL, USA
[f] School of Agriculture and Environment, University of Western Australia, Crawley, Western Australia, Australia
[g] School of Natural Resources, University of Nebraska-Lincoln, Lincoln, NE, USA
[h] Department of Environmental Sciences, University of Virginia, Charlottesville, Virginia, USA
[i] Department of Plant Sciences, University of California, Davis, California, USA
[j] Division of Geological and Planetary Sciences, California Institute of Technology, Pasadena, California, USA
[k] Jet Propulsion Laboratory, California Institute of Technology, Pasadena, California, USA
[l] Research Institute of Agriculture and Life Sciences, Seoul National University, Seoul, South Korea
[m] Department of Landscape Architecture and Rural Systems Engineering, College of Agriculture and Life Sciences, Seoul National University, South Korea
[n] National Center of Supercomputing Applications, University of Illinois at Urbana-Champaign, Urbana, IL, USA

ARTICLE INFO

Edited by Jing M. Chen

Keywords:
Solar-induced chlorophyll fluorescence (SIF)
Gross primary production (GPP)
SIF-GPP peak timing mismatch
Absorbed photosynthetic active radiation (APAR)
Canopy chlorophyll content (Chl_{Canopy})
Soybean

ABSTRACT

Recent advances in remotely sensed solar-induced chlorophyll fluorescence (SIF) have provided an exciting and promising opportunity for estimating gross primary production (GPP). Previous studies mainly focused on the linear correlation between SIF and GPP and the slope of the SIF-GPP relationship, both of which lack rigorous consideration of the seasonal trajectories of SIF and GPP. Here, we investigated the timing of seasonal peaks of far-red SIF and GPP in soybean fields by integrating tower data, satellite data, and process-based Soil Canopy Observation of Photosynthesis and Energy (SCOPE, v2.0) model simulations. We found inconsistency between the seasonal peak timing of far-red SIF and GPP in three of four soybean fields based on tower far-red SIF and eddy-covariance measurements. In particular, far-red SIF reached its seasonal maximum 14–17 days earlier than GPP. This far-red SIF-GPP difference in peak timing degraded the correlation between sunny-day far-red SIF and GPP at daily scale (Pearson $r = 0.83$–0.87 at the site with 14–17 days difference and Pearson $r = 0.96$ at the site with no difference), and it can be explained by a divergence in the seasonality between absorbed photosynthetic active radiation (APAR) and canopy chlorophyll content (Chl_{Canopy}). We found that the seasonality of far-red SIF - a byproduct of the light reactions of photosynthesis - was primarily controlled by APAR, whereas GPP seasonality was dominated by Chl_{Canopy}. Further, SCOPE model simulations showed that the seasonal patterns of leaf area index (LAI), leaf chlorophyll content (Chl_{Leaf}) and leaf angle distribution (LAD) could affect the different peak timing of SIF and GPP and consequently the seasonal relationship between far-red SIF and GPP. A further increase in LAI after the fraction of light absorption (FPAR) saturates and a later peak of Chl_{Leaf} compared to LAI results in a later peak of GPP compared to far-red SIF. More horizontal leaf angles can further exacerbate this difference. Our results advance mechanistic understanding of the SIF-GPP relationships and combining chlorophyll content information with SIF could potentially improve remote-sensing-based GPP estimation.

* Corresponding author at: Agroecosystem Sustainability Center, Institute for Sustainability, Energy, and Environment, University of Illinois at Urbana-Champaign, Urbana, IL, USA
E-mail addresses: chongya@illinois.edu, kaiyug@illinois.edu (K. Guan).

https://doi.org/10.1016/j.rse.2022.113104
Received 13 January 2022; Received in revised form 25 April 2022; Accepted 23 May 2022
Available online 6 June 2022

1. Introduction

Recent developments of solar-induced chlorophyll fluorescence (SIF) measurements from new and emerging remote sensing platforms may provide a promising way for estimating gross primary production (GPP) (Damm et al., 2010; Frankenberg et al., 2011; Guan et al., 2016; Guanter et al., 2014). SIF is an optical signal directly emitted by plants during the light reactions of photosynthesis in the spectral range of 650–800 nm and has the potential to directly assess ecosystem photosynthesis (Mohammed et al., 2019; Porcar-Castell et al., 2014; Ryu et al., 2019). Linear relationships between satellite-derived SIF and GPP have been reported in various ecosystems (Li et al., 2018; Sun et al., 2017), and some efforts have been made to solely use satellite SIF for GPP estimation at the regional (Guanter et al., 2014) and global scales (Li and Xiao, 2019; Zhang et al., 2020b). However, most satellite SIF products have coarse spatial and temporal resolutions (Frankenberg et al., 2011; Joiner et al., 2013; Wen et al., 2020), which causes the linearity between SIF and GPP likely to be linked to the spatial and temporal averaging (Li et al., 2020) and/or the integration of canopy structural and physiological processes (Magney et al., 2020). Several recent mechanistic studies from tower spectral measurements have found nonlinear relationships between SIF and GPP at finer spatiotemporal scales (He et al., 2020; Kim et al., 2021; Paul-Limoges et al., 2018; Tagliabue et al., 2019) and a decoupling of SIF and photosynthesis under stressed conditions (Helm et al., 2020; Marrs et al., 2020), which demonstrates the complexity of SIF-GPP relationships.

The mechanistic differences between SIF and GPP at both leaf and canopy scales may explain the complexity of SIF-GPP relationships. First, SIF is emitted during the light reactions of photosynthesis, and is regulated by photochemistry and heat dissipation during light absorption by chlorophyll molecules (Gu et al., 2019; Guan et al., 2016; Porcar-Castell et al., 2014). Photosynthesis, however, is affected by both light and carbon reactions since NADPH and ATP produced from the light reactions drive the carbon reactions for CO_2 assimilation in the stroma of chloroplasts which ultimately determines photosynthesis. Second, scaling both SIF and photosynthesis from the leaf to the canopy introduces additional factors. Observed top-of-canopy SIF is not simply the cumulative SIF of all leaves but is instead affected by light absorption, reabsorption and scattering within the canopy. This effect can be quantified by the escape probability (f_{esc}) which determines the fraction of SIF photons from all leaves escaping from the canopy (He et al., 2017; Yang and van der Tol, 2018; Zeng et al., 2019). Ecosystem GPP derived from eddy covariance measured net carbon flux (NEE), however, is the cumulated leaf-level photosynthesis from all leaves of the canopy.

The aforementioned differences between SIF and GPP are well characterized by the formulations of SIF and GPP in the light use efficiency (LUE) framework. For the observed top-of-canopy SIF, we have

$$SIF = APAR \times \Phi_F \times f_{esc} \quad (1)$$

where APAR is the absorbed photosynthetic active radiation (PAR) by the canopy, $\Phi_F$is the physiological total SIF emission yield of the canopy from the light reactions of photosynthesis, and f_{esc} is the escape probability. For observation-derived ecosystem GPP, we have

$$GPP = APAR \times LUE \quad (2)$$

where LUE is the photosynthetic light use efficiency of the canopy. LUE is affected by not only the photochemistry during the light reactions of photosynthesis, but also the physiological and diffusion processes during the carbon reactions of photosynthesis (Gu et al., 2019; Stocker et al., 2020). In addition, canopy structure also plays an important role in LUE, partly because it affects the light distribution within the canopy (Medlyn, 1998) and LUE can be higher under diffuse light conditions (Gu et al., 2002; Urban et al., 2007). When comparing the two equations for SIF and GPP, the differences between the light and carbon reactions are revealed by the SIF-APAR, GPP-APAR and Φ_F-LUE relationships, while f_{esc} represents an extra term for SIF to account for the canopy reabsorption and scattering effects, though the performance of f_{esc} might be influenced by sun-sensor geometry effects (Hao et al., 2022). Strong SIF-APAR relationships have been reported in many agro-ecosystems at both diurnal and seasonal scales, which are often stronger than GPP-APAR relationships (Miao et al., 2018; Yang et al., 2018a; Yang et al., 2021). This demonstrates that the observed SIF signal is dominated by APAR (with a smaller impact of Φ_F in these ecosystems) while both APAR and LUE are important for GPP. Meanwhile, weak correlations between apparent SIF yield ($\Phi_F \times f_{esc}$) and LUE as well as Φ_F and LUE have been shown in many agro-ecosystems (Dechant et al., 2020; Wu et al., 2019; Yang et al., 2018a). These result in the weaker SIF-GPP relationships compared to SIF-APAR in several agro-ecosystems (Dechant et al., 2020). After considering the f_{esc} correction, SIF from all leaves (SIF_{total}) shows even weaker correlations with GPP but stronger correlations with APAR compared to observed SIF, and almost no correlations between derived Φ_F and LUE were found, while f_{esc} showed considerable correlation to LUE (Dechant et al., 2020; Liu et al., 2020). All of these findings suggest that for crops: 1) both observed SIF and SIF_{total} are dominated by APAR, whereas GPP represents both light and carbon reactions; and 2) canopy structure plays a different role in observed SIF and GPP at the canopy scale. Indeed, recent leaf and canopy studies have revealed that GPP and SIF can be decoupled at fine spatiotemporal scales due to the effect of photorespiration (He et al., 2020; Magney et al., 2020) and stomatal regulation (Helm et al., 2020; Marrs et al., 2020) on LUE.

Close relationships between total canopy chlorophyll content (Chl_{Canopy}) and GPP have been found in croplands (Gitelson et al., 2006; Peng et al., 2011; Peng and Gitelson, 2012; Wu et al., 2009). Chl_{Canopy}, determined as the product of leaf chlorophyll content (Chl_{Leaf}) and total leaf area index (LAI), can be estimated by radiative transfer models (Darvishzadeh et al., 2008; Delloye et al., 2018; Weiss and Baret, 2016) or vegetation indices (Dash and Curran, 2004; Gitelson et al., 2005; Inoue et al., 2016) from canopy reflectance, which allows GPP to be estimated using chlorophyll-related indices and PAR (Gitelson et al., 2012; Wu et al., 2009). The strong correlations between Chl_{Canopy} and GPP can be explained in two ways. First, the fraction of absorbed PAR by the canopy (FPAR) is linearly correlated with low-to-moderate Chl_{Canopy} since LAI determines how many leaves available for light absorption and chlorophylls are the major pigments to absorb light (Thenkabail et al., 2011). Second, although FPAR saturates at high Chl_{Canopy} conditions, e.g., 2 g m^{-2} for maize (Peng et al., 2011), LUE increases with the increase of Chl_{Canopy}, largely because Chl_{Leaf} is strongly correlated with the maximum carboxylation rate (V_{cmax}) due to the sharing of the photosynthetic nitrogen pool (Croft et al., 2017; Houborg et al., 2015b; Lu et al., 2020; Wang et al., 2020c) which is important for LUE when GPP is not limited by light (Stocker et al., 2020; Wang et al., 2017). The correlation between Chl_{Canopy} and LUE ensures that GPP still remains sensitive to moderate-to-high Chl_{Canopy} (Peng et al., 2011; Thenkabail et al., 2011). On the other hand, for far-red SIF which is commonly used in remote sensing studies, similar to GPP, LAI nonlinearly determines FPAR which affects SIF, but far-red Φ_F and f_{esc} are insensitive to Chl_{Leaf} at normal-to-high Chl_{Leaf} conditions (Dinç et al., 2012; Tubuxin et al., 2015; Yang and van der Tol, 2018). Therefore, Chl_{Canopy} strongly relates to FPAR and LUE, both of which are important for GPP, but weakly relates to far-red Φ_F and f_{esc}, suggesting that Chl_{Canopy} could potentially capture seasonal variations of GPP better than far-red SIF.

In this study, we aim to investigate the seasonal maximum of far-red SIF and GPP in soybean fields by integrating tower measurements, satellite data, and model simulations. Previous studies have mainly investigated SIF-GPP relationships through calculating their regression slope and coefficient of determination (R^2). Although some studies have found that far-red SIF is able to capture the GPP-based phenophase transitions at the start and end of the growing season (Lu et al., 2018; Wang et al., 2020b), the seasonal peaks of far-red SIF and GPP remain less investigated, which hampers our understanding of the SIF-GPP relationships. Soybean is a typical C3 crop for which LUE contribution to GPP variation

is important (Gitelson et al., 2015, 2018; Wu et al., 2020). It is also one of the major harvested crops around the world and plays critical roles in global food security, agricultural economy and biofuel production (Ainsworth et al., 2012; Long et al., 2006; Van Gerpen and Knothe, 2008). Specifically, we propose the following questions: Do soybean far-red SIF and GPP reach a seasonal peak at a similar time? If not, what causes the difference in seasonal trajectories of far-red SIF and GPP? We hypothesize that the seasonal peak timing of far-red SIF and f_{esc}-corrected SIF_{total} are determined by the timing of APAR, while the seasonal maximum of GPP is determined by the timing of Chl_{Canopy}. Thus, whether soybean far-red SIF and GPP reach their respective peaks at a similar time will depend on the seasonal peak timing of APAR and Chl_{Canopy}.

2. Materials and methods

We thoroughly tested our hypotheses using tower data at four sites in the U.S. Corn Belt and satellite data at two US counties, with each county land area representing ~2000 km^2. The location of the field sites and counties are shown in Fig. S1. Process-based model simulations are conducted at the site level to further understand the underlying mechanism of the seasonal peak timing difference between far-red SIF and GPP. As fluctuations in cloud cover could affect the seasonal peak detection for far-red SIF and GPP, we focused on clear-sky conditions in this study. An overview of the tower data, satellite data and process-based model simulations is shown in Fig. 1 and detailed descriptions about each dataset acquisition are given in the following subsections.

2.1. Tower data

2.1.1. Study sites

Tower data from four soybean sites were used for the site-level analysis (Table 1). These sites were all located in the U.S. Corn Belt, with one site (BR3, rainfed, corn-soybean rotation, 41.9745°N, 93.6937°W) at the National Laboratory for Agriculture and the Environment in Iowa (Dold et al., 2019), two sites (NE2, irrigated, corn-soybean rotation, 41.1649°N, 96.4701°W, and NE3, rainfed, corn-soybean rotation, 41.1797°N, 96.4397°W) at the Eastern Nebraska Research and Extension Center of University of Nebraska-Lincoln in Nebraska, and the other site (UIUC, rainfed, corn-corn-soybean rotation, 40.0628°N, 88.1959°W) at the Energy Farm of University of Illinois at Urbana-Champaign. At all four sites, soybean was planted in May and harvested in October. Tower data was collected in 2017 at the BR3 site, in 2018 at the NE2 and NE3 sites, and in 2019 at the UIUC site.

Table 1
Overview of the four field datasets with a focus on far-red SIF observations. DOY: day of year. FOV: field of view. DOAS: Differential Optical Absorption Spectroscopy. iFLD: improved Fraunhofer Line Depth.

Site	Spectral system	View angle	SIF retrieval method	Data availability	Latitude/ Longitude
BR3	PhotoSpec	Nadir to the horizon in 0.7° steps at two azimuth angles (−45° and 60°)	DOAS	Jun 14 – Sep 8, 2017 (DOY 165–251, 2017)	41.9745/ −93.6937
NE2	Fluospec2	Nadir with 25° FOV	iFLD	Jun 19 – Oct 14, 2018 (DOY 170–287, 2018)	41.1649/ -96.4700
NE3	Fluospec2	Nadir with 25° FOV	iFLD	Jul 8 – Oct 14, 2018 (DOY 189–287, 2018)	41.1797/ -96.4397
UIUC	Fluospec2	Nadir with 25° FOV	iFLD	Jun 9 – Oct 10, 2019 (DOY 160–283, 2019)	40.0628/ -88.1950

2.1.2. Spectral measurements

Fluospec2 systems (Miao et al., 2018; Yang et al., 2018b) were installed atop of a 5-m tower at the NE2 site, the NE3 site and the UIUC site for spectral data collection. Each Fluospec2 has two subsystems: a

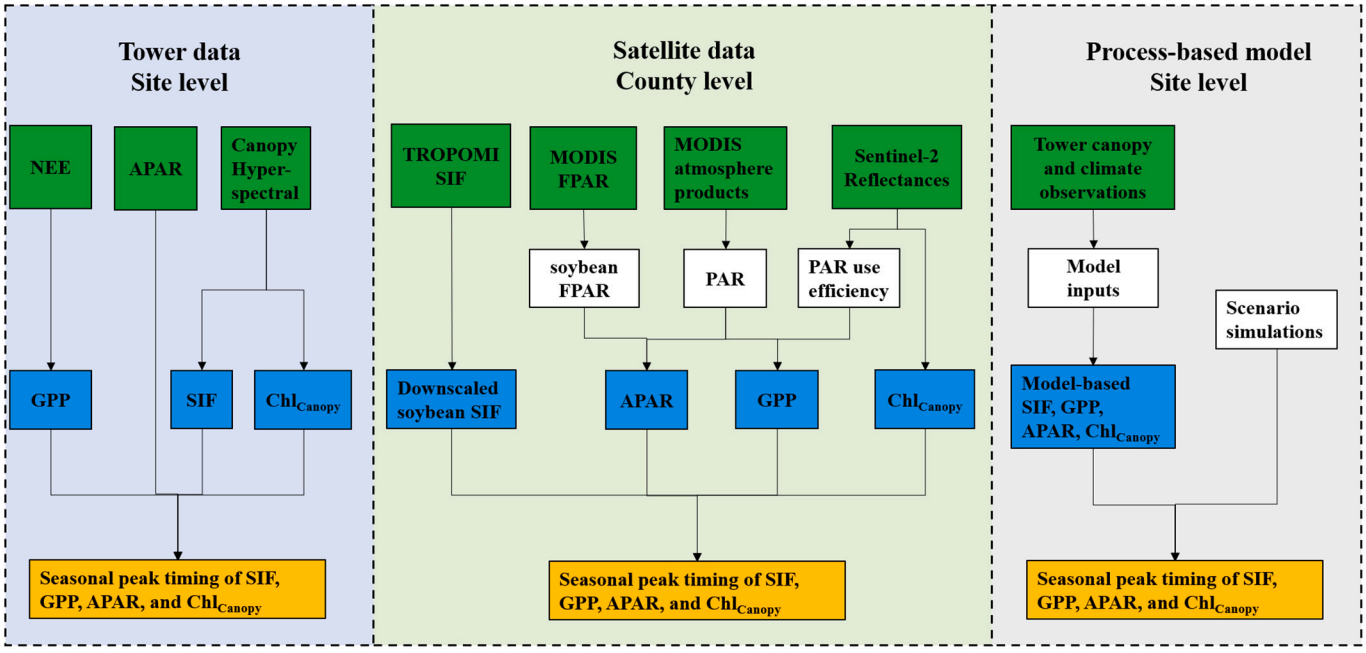

Fig. 1. Overview of the tower data, satellite data and process-based model simulations to investigate the seasonal peak timing of far-red SIF, GPP, APAR and Chl_{Canopy}. Data in the green box are tower and satellite observations and data in the blue box are outputs. Additional symbols are as follows: NEE: net ecosystem exchange; PAR: photosynthetic active radiation; FPAR: fraction of absorbed PAR of the canopy; TROPOMI: TROPOspheric Monitoring Instrument; MODIS: Moderate Resolution Imaging Spectroradiometer. (For interpretation of the references to colour in this figure legend, the reader is referred to the web version of this article.)

SIF subsystem equipped with a QE Pro spectrometer (Ocean Optics, Dunedin, FL, USA) covering the far-red SIF retrieval range (730–780 nm) at a high spectral resolution (0.15 nm), and a spectral observation subsystem equipped with a HR2000+ spectrometer (Ocean Optics, Dunedin, FL, USA) covering the visible-near infrared range (400–1100 nm) at a moderate spectral resolution (1.1 nm). Each subsystem uses two fibers to collect dowelling solar irradiance and upwelling canopy radiance separately, both in nadir direction with a 25° field of view and at a 5-min time interval. Far-red SIF at 760 nm was retrieved from the SIF subsystem using the improved Fraunhofer Line Depth (iFLD) method (Alonso et al., 2008; Cendrero-mateo et al., 2019). To clarify, only far-red SIF was used in this study. More details about the Fluspec2 measurement sequence and SIF retrieval can be found in Wu et al. (2020).

A PhotoSpec system (Grossmann et al., 2018; Magney et al., 2019; He et al., 2020) was installed atop of a 7-m tower at the BR3 site for spectral data collection. PhotoSpec consists of three commercial spectrometers. Two QE Pro spectrometers (Ocean Optics, Dunedin, FL, USA) cover the red (650–712 nm) and far-red (729–784 nm) SIF retrieval ranges at high spectral resolution (0.3 nm). The third Flame spectrometer (Ocean Optics, Dunedin, FL, USA) covers the visible-near infrared range (177–874 nm) at moderate spectral resolution (1.2 nm) (Grossmann et al., 2018). These spectrometers are mounted on a scanning telescope unit, enabling multi-angular observations from nadir to 45° view zenith angle at two azimuth angles (−45° and 60°). More details about the PhotoSpec instrument and measurement sequence can be found in Grossmann et al. (2018) and Magney et al. (2019). Far-red SIF retrieval followed the established Differential Optical Absorption Spectroscopy (DOAS) method (Platt, 2017), which detects optical density changes within solar Fraunhofer lines. More details about far-red SIF retrieval can be found in Grossmann et al. (2018). The averaged far-red SIF retrieved from a 745–758 nm window over all viewing angles, which can be considered as a hemispherical far-red SIF, was used in this study. The spectral measurements for far-red SIF at four sites are summarized in Table 1. PhotoSpec and Fluspec2 have different instrumentation setups and different methods were used for far-red SIF retrieval which might cause some uncertainty when comparing them directly. However, this study mainly focuses on the seasonal pattern of far-red SIF under clear days rather than the absolute magnitude. Different retrieval methods have less impact on far-red SIF under clear days (Chang et al., 2020). Additionally, the three Fluospec2 sites, NE2, NE3, and UIUC, are the major focus of this study, whereas the PhotoSpec site BR3 is used to support other three sites. We intended to investigate the seasonal patterns of far-red SIF and GPP across sites using different measurement systems and retrieval methods to examine whether the results were consistent.

2.1.3. GPP estimation from Eddy covariance (EC) data

GPP data were acquired from eddy covariance (EC) towers that were located in the same field as the spectral systems at each site. Each EC system included a sonic anemometer and a CO_2/H_2O infrared gas analyzer. Auxiliary measurements of meteorological variables close to the EC system such as air temperature, relative humidity and radiation were also measured at each site. Detailed information on the EC instrumentation can be found in (Dold et al., 2017, 2019) for the BR3 site, in (Suyker and Verma, 2012) for the NE2 and NE3 sites, and in (Moore et al., 2020) for the UIUC site.

Raw 10 Hz CO_2 and wind turbulence data were processed to derive half-hourly Net Ecosystem Exchange (NEE) using the EddyPro software (version 6.2.0, LI-COR, Lincoln, NE, USA), which applied a rotation tilt correction (double rotation), time-lag compensation (covariance maximization), density fluctuation compensation (Webb et al., 1980), flux de-trending (block average), spectral correction (Moncrieff et al., 1997, 2005) and spikes detection and removal (Vickers and Mahrt, 1997). NEE data from unfavorable conditions, such as rain days and low turbulent mixing conditions, were filtered and outliers were also excluded. The remaining NEE dataset was gap-filled together with tower ancillary meteorological data of shortwave radiation, air or soil temperature, and vapor pressure deficit followed the procedure proposed by Papale et al. (2006) and Reichstein et al. (2005). Gap-filled NEE was then partitioned into GPP and ecosystem respiration (ER) using the standard night-time partitioning method (Reichstein et al., 2005), for which nighttime NEE was assumed to represent ER and was used to develop a respiration-temperature model for the daytime ER estimation. Details on GPP data processing can be found in (Magney et al., 2019) for the BR3 site, and an open-source eddy covariance processing pipeline ONEFlux was used to estimate GPP at NE2, NE3 and UIUC sites (Pastorello et al., 2020).

2.1.4. Correcting nadir-view far-red SIF observations to EC footprint

GPP footprint changes with wind direction and covers a larger area compared to nadir-view far-red SIF observations (Liu et al., 2017), which might cause uncertainty in the seasonality comparison between far-red SIF and GPP. To address this issue, we used the product of near-infrared reflectance of vegetation (NIRv) and PAR (NIRvP) as a proxy for far-red SIF to upscale SIF observations from small nadir footprints to large GPP footprints. Cross-scale studies have shown that NIRvP can explain around 80% variation of far-red SIF (Dechant et al., 2022; Kimm et al., 2021). To further reduce the soil background impact on NIRv, soil-adjusted NIRv (SANIRv) was further calculated following the method in Jiang et al. (2020) and used for far-red SIF footprint correction. By detecting and removing soil NIRv from time series NIRv observations on a pixel basis, SANIRv reduces NIRv value when vegetation is sparse and reaches 0 at the absence of vegetation, while it does not change NIRv value when vegetation is dense. Daily SANIRv was used as all half-hourly SANIRv within that day. Details of EC footprint and SANIRv calculation can be found in supplementary materials. GPP footprint-based far-red SIF at each half-hour ($SIF_{GPP\ footprint}$) was calculated from nadir-view far-red SIF observations ($SIF_{obs,\ halfhour}SIF_{obs}$) based on the following equations:

$$SIF_{GPP\ footprint} = SIF_{obs} \times Ratio$$

$$Ratio = \frac{SANIRv_{GPP\ footprint} \times PAR_{GPP\ footprint}}{SANIRv_{SIF\ pixel} \times PAR_{SIF\ pixel}} \approx \frac{SANIRv_{GPP\ footprint}}{SANIRv_{SIF\ pixel}}$$

$$SANIRv_{GPP\ footprint} = \sum_{i=1}^{N} w_i \times SANIRv_i \quad (3)$$

where $SANIRv_{GPP\ footprint}$, $SANIRv_{SIF\ pixel}$, $PAR_{GPP\ footprint}$ and $PAR_{SIF\ pixel}$ are GPP-footprint-weighted SANIRv, SIF-tower-pixel SANIRv, GPP-footprint-weighted PAR, and SIF-tower-pixel PAR, respectively. $PAR_{GPP\ footprint}$ and $PAR_{SIF\ pixel}$ were assumed identical. N is the total number of pixels within the GPP footprint. w_i is the GPP contribution of the *i*th pixel to the footprint GPP calculated by footprint models. $SANIRv_i$ is the SANIRv value of the *i*th pixel. SIF footprint correction was not conducted at BR3 site due to the lack of SAFE model inputs and the larger observation zenith angle coverage (scans from nadir to the horizon in 0.7° steps at two azimuth angles) of PhotoSpec observations. Overall, corrected GPP footprint based far-red SIF followed similar seasonal patterns as the observed nadir-view GPP at NE2, NE3 and UIUC sites (Fig. S2). Direct far-red SIF observations at BR3 and corrected GPP footprint-based far-red SIF at NE2, NE3 and UIUC were used for later analysis, with the same variable "far-red SIF" for the sake of simplicity.

2.1.5. APAR, LAI, Chl_{Canopy}, and SIF_{total} estimation

At the NE2, NE3 and UIUC sites, incoming PAR (PAR_{in}) was measured by point quantum sensors (LI-COR Inc., USA) pointing upward placed at 5 m above the ground; reflected PAR from the canopy and soil (PAR_{out}) was measured by point quantum sensors (LI-COR Inc., USA) pointing downward at 5 m from the ground; transmitted PAR through the canopy (PAR_{trans}) was measured by line quantum sensors (LI-COR Inc., USA) viewing upward placed at ~2 cm above the ground. From these measurements, FPAR and APAR were derived at half-hourly intervals.

$$APAR = PAR_{in} - PAR_{out} - PAR_{trans}$$

$$FPAR = \frac{APAR}{PAR_{in}} \quad (4)$$

At the BR3 site, due to the absence of direct FPAR measurements, APAR was estimated by multiplying NDVI, which has commonly been used as a measure of FPAR, and PAR following the method of Magney et al. (2019). Total LAI was measured at the NE2 and NE3 sites using the destructive method (Kira et al., 2017) and was measured by a LI-2200C plant canopy analyzer (LI-COR, Lincoln, NE, USA) at the UIUC site.

Canopy chlorophyll content Chl_{Canopy} was estimated by the Red-edge chlorophyll index ($CI_{rededge}$) from the canopy hyperspectral reflectance following the equation from Gitelson et al. (2005):

$$Chl_{Canopy} = 0.4124 \times CI_{rededge} - 0.1117 \quad (5)$$

Although $CI_{rededge}$ mainly accounts for the top canopy chlorophyll content, Gitelson et al. (2006) have demonstrated that total chlorophyll of a soybean canopy can be accurately estimated by the upper canopy chlorophyll content. This $CI_{rededge}$-based Chl_{Canopy} estimation has been widely used in crop GPP estimation (Gitelson et al., 2012; Wu et al., 2009).

SIF_{total} from all leaves was estimated through dividing the far-red SIF by the escape ratio f_{esc} which can be estimated from near-infrared reflectance from vegetation (NIR_v) and FPAR following the approach proposed by (Zeng et al., 2019):

$$f_{esc} = \frac{NIR_v}{FPAR}$$

$$SIF_{total} = SIF/f_{esc} \quad (6)$$

This method has been validated with comprehensive radiative transfer simulations and satellite observations (Zeng et al., 2019). To account for the footprint mismatch between far-red SIF and GPP at the NE2, NE3 and UIUC sites, NIRv was corrected to GPP footprint weighted NIRv using the ratio calculated from section 2.1.4. The equations of the vegetation indices (VIs) that were used in this subsection are listed in Table 2.

2.2. Satellite data

In addition to tower data at the study sites, we further investigated the seasonal trajectories of soybean far-red SIF, GPP, APAR and Chl_{Canopy} derived from multi-satellite data at two counties: Saunders County in Nebraska where the NE2 and NE3 sites are located in 2018 and Champaign County in Illinois where the UIUC site is located in 2019 (Fig. S1).

2.2.1. Soybean APAR and far-red SIF estimation

We derived an 8-day clear-sky soybean APAR dataset by multiplying clear-sky PAR by soybean FPAR. Daily clear-sky PAR was derived by upscaling ground observations from the SURFRAD network to the regional scale using multiple machine learning approaches (Jiang et al., 2020). 8-day soybean FPAR was derived by unmixing landscape FPAR in the MCD15A2H LAI/FPAR product(Text S2). This APAR dataset was aggregated to 4 km-resolution grids. We further derived an 8-day 4 km-resolution clear-sky soybean far-red SIF dataset by unmixing landscape far-red SIF retrievals from TROPOspheric Monitoring Instrument (TROPOMI) onboard the Sentinel-5 Precursor satellite (Text S2). The TROPOMI far-red SIF was retrieved from spectral measurements in the range of 743–758 nm, with a footprint size of about 7 km × 3.5 km and at a daily interval (Köhler et al., 2018). TROPOMI footprints with cloud coverage ≥0.3 were excluded from the analysis (Wang et al., 2020a). The land cover unmixing algorithm assumed SIF yield of a specific land cover (corn, soybean, forest or grass) was invariant at local scale, and solved the land cover specific SIF yield using land cover specific APAR, fraction of individual land cover types, and TROPOMI far-red SIF within a certain area (e.g., a county). The soybean far-red SIF was therefore calculated as the product of soybean APAR and soybean SIF yield (Text S2). Finally, we calculated the county-level soybean APAR and far-red SIF by averaging soybean APAR and far-red SIF across all 4 km pixels within the county. Detailed information about the soybean FPAR and far-red SIF derivation algorithms can be found in the supplementary materials (Text S2). SIF_{total} was not estimated for satellite far-red SIF considering the uncertainty of MODIS FPAR for f_{esc} calculation using Eq. (6) (Zeng et al., 2019).

2.2.2. Soybean GPP and Chl_{Canopy} estimations

We derived a daily clear-sky GPP dataset by upscaling ground observations from the study sites to the regional scale using a machine learning approach. Specifically, we calculated incident PAR use efficiency (iPUE = GPP/PAR (Jiang et al., 2020) using EC-derived daily mean soybean GPP and PAR at the NE2, NE3 and UIUC sites as ground truth, and we used daily surface reflectance at 10 Sentinel-2 bands (Band 2, 3, 4, 5, 6, 7, 8, 8a, 11 and 12) as inputs, to train a least absolute shrinkage and selection operator (LASSO) model. The derivation of daily surface reflectance dataset can be found in supplementary materials. We applied the trained model to all Sentinel-2 data to upscale EC-derived iPUE to the county scale, and multiplied by clear-sky PAR (Section 2.2.1) to obtain daily clear-sky soybean GPP at 10 m resolution.

Chl_{Canopy} was calculated from daily 10 m-resolution Sentinel-2 surface reflectance data using Eq. (5), where $CI_{rededge}$ (Table 2) was calculated using Sentinel-2 red and a red edge band, corresponding to that derived from the Fluospec2 system. Both daily GPP and Chl_{Canopy} were averaged to 8-day to match APAR and far-red SIF (Section 2.2.1) data.

2.3. Process-based modeling

To verify our hypothesis that the seasonal peak timing difference of far-red SIF and GPP is a result of the peak timing difference of APAR-Chl_{Canopy}, we further employed a process-based modeling approach to investigate the seasonal trajectories of soybean far-red SIF, GPP, APAR and Chl_{Canopy}. We first conducted site-level simulations to evaluate the model performance in reconstructing seasonal trajectories at the study sites, and subsequently conducted several scenario simulations to reveal the underlying mechanism.

2.3.1. Far-red SIF, GPP, APAR and Chl_{Canopy} estimations

We used the Soil Canopy Observation of Photosynthesis and Energy (SCOPE) model to investigate the seasonal trajectories of soybean far-red SIF, GPP, APAR and Chl_{Canopy}. SCOPE v2.0 is a 1-D model capable of simulating radiative transfer, energy balance, and photosynthesis, as well as the SIF of individual leaves within the canopy and total emitted SIF across the full spectrum of chlorophyll fluorescence (Van Der Tol et al., 2009; Yang et al., 2020). It has been widely used to explore the relationship between GPP and SIF from a mechanistic perspective (Celesti et al., 2018; Van Der Tol et al., 2014; Verrelst et al., 2015). We

Table 2
Tower vegetation indices (VIs) used in this study. R_{red} and $R_{red\ edge}$ refer to reflectance derived from spectral data collected by the broadband reflectance subsystem of the PhotoSpec and Fluospec2 system in bands of 650–660 nm and 703.75–713.75 nm, respectively. R_{NIR} is the near-infrared reflectance and it refers to the average of 770–780 nm in NDVI calculation and average of 750–757.5 nm in $CI_{rededge}$ calculation.

Vegetation index	Formula	Reference
Normalized difference vegetation index (NDVI)	$(R_{NIR} - R_{red})/(R_{NIR} + R_{red})$	Rouse et al. (1973)
Red edge chlorophyll index ($CI_{rededge}$)	$R_{NIR}/R_{red\ edge} - 1$	Gitelson et al. (2005)
Near-infrared reflectance of vegetation (NIR_v)	$NDVI * R_{NIR}$	Badgley et al. (2017)

first retrieved unmeasured vegetation variables using a model inversion approach constrained by observed tower data, and then estimated SIF, GPP, APAR and Chl_{Canopy} using SCOPE driven by observed and retrieved tower data (Fig. A1 and Table A1). SCOPE modelling was not conducted at the BR3 site due to the absence of direct LAI and FPAR measurements.

Six of the SCOPE forcings (leaf chlorophyll content Chl_{Leaf}, leaf carotenoid content C_{ca}, leaf dry matter content C_{dm}, leaf thickness parameter N, and leaf inclination distribution function parameters LIDFa and LIDFb) were retrieved from tower observed hyperspectral reflectance and FPAR. We coupled a canopy radiative transfer model PROSAIL with a look-up table (LUT) method to conduct the retrieval. Specifically, we established 5180 databases, with LAI ranging from 0.1 to 7.0 at 0.1 interval and solar zenith angle ranging from 17 to 80 at 1 degree interval, by running PROSAIL with sampled parameter values listed in Table A2. We employed a two-step strategy to estimate Chl_{Leaf}, C_{ca}, C_{dm} and N at daily interval and leaf angle distribution (LAD) type (Planophile, Erectophile, Plagiophile, Extremophile, Spherical, or Uniform) at 30 min interval considering that soybean LAD has a diurnal variation. For each 30 min timestamp, we first used the known LAI which was temporally interpolated from field measurements and the calculated solar zenith angle to select the relevant database. Then we compared observed hyperspectral reflectance R and FPAR with records in the simulated database and calculated the simulation error by:

$$\varepsilon = \sqrt{\frac{1}{l}\sum_{\lambda=1}^{l}\left[R_{observation}(\lambda) - R_{simulation}(\lambda)\right]^2} + \left|FPAR_{observation} - FPAR_{simulation}\right| \quad (7)$$

where $\lambda = 1,2,\ldots,l$ indicates band number and $l = 321$ corresponding to 460–780 nm with 1 nm interval. We chose the top 1% small ε simulations in the database and considered the average of corresponding parameter values as the solution for the five parameters (Weiss et al., 2000). Subsequently, we applied a Savitzky–Golay filter to the time series of midday retrieval for Chl_{Leaf}, C_{ca}, C_{dm} and N to derive daily retrievals. Then we refined the LAD type retrieval by minimizing ε (Eq. (9)) for each 30 min timestamp. Since the six LAD types are predefined in the same manner in PROSAIL and SCOPE, corresponding LIDFa and LIDFb parameters were obtained from the PROSAIL retrieval and used for SCOPE.

We used the PROSAIL-retrieved Chl_{Leaf} to estimate V_{cmax} considering that Chl_{Leaf} is strongly correlated with Rubisco content which has close correspondence with V_{cmax}, and the strong correlation between Chl_{Leaf} and V_{cmax} at seasonal scale has been demonstrated in winter wheat and a temperate forest (Lu et al., 2020). Herein we used the empirical linear relationship between V_{cmax} and Chl_{Leaf} from Houborg et al. (2015a):

$$V_{cmax} = 1.75 \times C_{ab} - 10.1 \quad (8)$$

Once all parameters were optimized for each site, they were combined with field-measured LAI and meteorological data (shortwave radiation R_{in}, longwave radiation R_{li}, air temperature T_a, ambient water vapor e_a, air pressure P_a, wind speed u, and ambient CO_2 concentration C_a) as SCOPE forcing, and SIF at 760 nm, GPP and APAR were predicted by running SCOPE at half-hourly interval. SCOPE SIF_{total} was not estimated using Eq. (4) but directly output by SCOPE model. To be consistent with tower measurements, APAR from SCOPE was the total APAR rather than APAR from chlorophylls. SCOPE-estimated Chl_{Canopy} was calculated as the product of field-measured LAI and PROSAIL-retrieved Chl_{Leaf}, since Chl_{Leaf} in PROSAIL is the average of the canopy.

2.3.2. Model simulation scenarios

In addition to the simulations of far-red SIF, GPP, APAR and Chl_{Canopy} using the observed and retrieved tower data, we also conducted scenario simulations to identify the key factors that determine the SIF-GPP with regards to peak dates. Considering APAR or FPAR is mainly affected by canopy structure variables such as LAI and LAD (Huemmrich, 2013; Myneni and Williams, 1994), whereas Chl_{Canopy} is determined by LAI and Chl_{Leaf} (Gitelson et al., 2005), we set up different scenarios by varying LAI, LAD and Chl_{Leaf} while keeping other SCOPE model parameters constant. Specifically, we assumed the seasonal trajectories of LAI and Chl_{Leaf} follow the Gaussian distribution:

$$x = ae^{-\left(\frac{DOY-b}{c}\right)^2} \quad (9)$$

where x could be either LAI or Chl_{Leaf}, a is the maximum value of x over the season, b is the DOY when x reaches its peak over the season, and c is a shape parameter controlling the seasonality of x. A larger c indicates a broader seasonal trajectory whereas a smaller c indicates a narrower seasonal trajectory (Fig. S3). We set $a = 4.5\ m^2\ m^{-2}$ for LAI and 75 μg cm^{-2} for Chl_{Leaf}, b = DOY 200, 220, or 240, and c = 30 and 60, respectively. We considered three distinct LAD types: Planophile (dominated by relatively horizontal leaves), Spherical and Erectophile (dominated by relatively vertical leaves). Consequently, a total of 6 LAI seasonal trajectories × 6 Chl_{Leaf} seasonal trajectories ×3 LAD types = 108 scenarios were involved in the simulation. We fixed all other vegetation variables, and used mean clear-day diurnal cycles of NE2, NE3 and UIUC for all environmental variables except for shortwave radiation R_{in} (Table A1). For R_{in}, we calculated it as $R_{in} = R_{TOA} \times T_R$ where R_{TOA} is the shortwave radiation at top of atmosphere which is a function of location and time and T_R is the mean clear-day diurnal cycle of atmospheric transmittance of the three study sites.

2.4. Data analysis

Time series of sunny-day mean values of far-red SIF, GPP, APAR, Chl_{Canopy} and SIF_{total} were used to detect their seasonal peaks at the four field sites. Considering the uncertainties under low light conditions in early morning and late afternoon, only data from 8:00 am to 6:00 pm (local standard time) were used to calculate the daily mean values for all variables. Only sunny-day data were used for the seasonal peak detection to avoid large fluctuations under cloudy conditions (Zhang et al., 2020a). Sunny days and cloudy days were distinguished by the ratio of actual PAR to theoretical PAR which was calculated from dates and solar zenith angles (Weiss and Norman, 1985). We first calculated the ratio at half hourly scale, and half-hourly period was defined as sunny when the ratio was above the threshold (0.6 for BR3, 0.65 for UIUC sites, 0.7 for NE2 and NE3 sites). Sunny day was then defined when more than 75% of the half-hourly period between 8:00 am to 6:00 pm was sunny. Different ratio thresholds were used to ensure enough sunny-day data remained for the peak detection with the consideration of different sky conditions across sites. A total of 36, 48, 41 and 45 sunny days were used for later analysis at the BR3, NE2, NE3 and UIUC sites, respectively. This sunny-day criterion was also applied to the SCOPE estimations, and the SCOPE-estimated sunny-day mean far-red SIF, GPP, APAR and Chl_{Canopy} from 8:00 am to 6:00 pm (local standard time) were calculated at each field site. For satellite data, only clear-sky PAR, APAR, far-red SIF and GPP were derived used for analysis.

For tower data, satellite data and SCOPE estimations, four methods were used to fit the seasonal trajectories of far-red SIF, GPP APAR and Chl_{Canopy} for the identification of their peak dates. The four methods were double logistic regression (DLR, Beck et al., 2006), Gaussian Process Regression (GPR, Belda et al., 2020), Kernel Ridge Regression (KRR, Belda et al., 2020) and Whittaker smoother (Eilers, 2003). KRR showed poor performance in smoothing APAR and SIF_{total} at the UIUC site, therefore KRR was not used in those cases. Because these methods showed similar performances in trajectory fitting at the four tower sites (Fig. S4), the mean fitted seasonal trajectories derived from the four methods were used to reduce the uncertainty caused by different smoothing methods. The peak dates were identified as the dates with maximum values in the fitted seasonal trajectories. For the UIUC site, a heatwave happened around DOY 200 (Fig. S5), and to avoid the heatwave influence data from DOY 195 to 205 was removed for the peak

detection. To test our hypothesis, the Pearson *r* was used to investigate the relationship between the DOY of far-red SIF peak and DOY of APAR peak, between the DOY of GPP peak and DOY of Chl_{Canopy} peak, between far-red SIF and GPP, between far-red SIF and APAR and between GPP and Chl_{Canopy}. Statistical significance of the correlation was evaluated with a two-sided *t*-test at a confidence level of 95%. Statistical analysis was done using the programming language Matlab.

3. Results

3.1. Seasonal variations of far-red SIF, GPP, APAR and Chl_{Canopy} from tower data

A difference in seasonal peak timing between far-red SIF and GPP was observed at the BR3, NE2 and NE3 sites (Fig. 2a-d). At these sites, far-red SIF reached peaks (DOY 212, 204 and 203 at BR3, NE2 and NE3, respectively) earlier than GPP (DOY 219–226). The seasonal peak timing difference between GPP and far-red SIF was the largest at the NE3 site (17 days), followed by NE2 (15 days) and BR3 (14 days). However, far-red SIF and GPP reached their peaks at the similar dates at UIUC (far-red SIF DOY: 220; GPP DOY: 221), different from the other three sites. Similar to the far-red SIF-GPP peak timing difference, a seasonal peak timing difference between APAR and Chl_{Canopy} was also observed at the BR3, NE2 and NE3 sites (Fig. 2e-h). At these sites, APAR generally reached peaks earlier than Chl_{Canopy} (DOY 207–214 vs. DOY 221–233). At the UIUC site, however, APAR and Chl_{Canopy} reached their peaks at similar times (APAR: DOY 222, Chl_{Canopy}: DOY 227). Overall, the peak dates were similar between far-red SIF and APAR, and between GPP and Chl_{Canopy}. The escape probability correction of SIF_{total} did not change the overall pattern, and they still showed earlier peaks compared to GPP at the BR3, NE2 and NE3 sites (Fig. 2i-l) due to the relatively stablef_{esc} at the peak growing season(Fig. S6).

3.2. Relationships between far-red SIF, GPP, APAR and Chl_{Canopy} from tower data

The difference in peak timing of far-red SIF and GPP affected the seasonal relationship between far-red SIF and GPP at a daily scale, especially on sunny days (Fig. 3). far-red SIF was less correlated with GPP at the three sites with differences in peak timing of far-red SIF and GPP were observed ($r = 0.83$–0.87 on sunny days, Fig. 3b), while the strongest relationship between far-red SIF and GPP was found at the UIUC site where far-red SIF and GPP reached peak maxima at the similar times ($r = 0.96$ on sunny days, Fig. 3d). The correlation between far-red SIF and GPP on all days was similar across four sites ($r = 0.85$–0.89). On both sunny days and all days, far-red SIF generally showed a stronger relationship with APAR compared to Chl_{Canopy}, and GPP generally showed a stronger relationship with Chl_{Canopy} than APAR at the four sites (Fig. 4; Fig. B1). After f_{esc} correction, SIF_{total} showed a stronger correlation with APAR but even weaker correlation with GPP (Fig. S7).

3.3. Seasonal variations of far-red SIF, GPP, APAR, Chl_{Canopy} from satellite data

Seasonal peak timing difference between far-red SIF and GPP (14 days) was observed in Saunders County in 2018 where the NE2 and NE3 sites were located using TROPOMI-derived soybean far-red SIF and Sentinel-2 derived soybean GPP data, but smaller difference (5 days) was observed in Champaign county in 2019 where the UIUC site was located (Fig. 5), consistent with that observed at the NE2 and NE3 sites using tower data (Fig. 2). Specifically, satellite-derived far-red SIF reached its peak at DOY 200), earlier than satellite-derived GPP which peaked at DOY 214 in Saunders County in 2018, while in Champaign county in 2019, far-red SIF reached the peak at DOY 224 and GPP reached peak at 229. Similarly, MODIS-derived APAR reached its peak (DOY 203) earlier than Sentinel-2 derived Chl_{Canopy} (DOY 221) in Saunders County in 2018, while satellite-derived APAR and Chl_{Canopy}

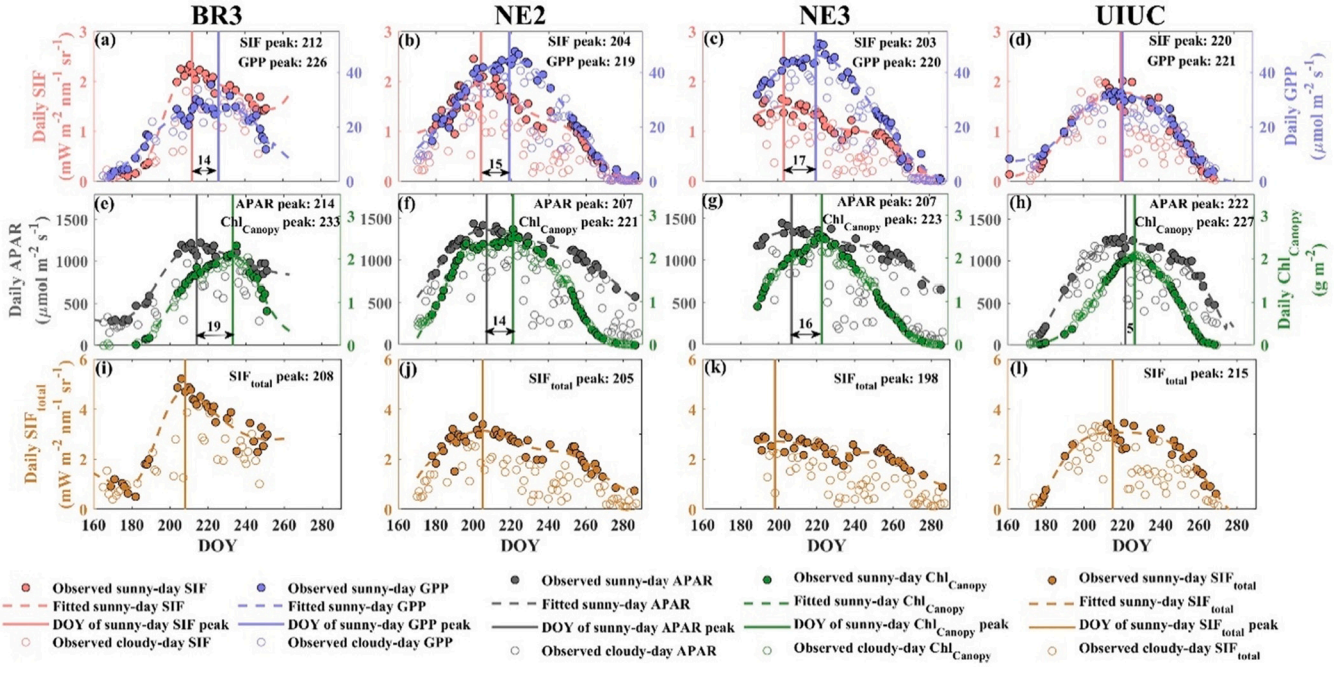

Fig. 2. Seasonal variations of daytime mean far-red SIF (red circles), GPP (blue circles), APAR (grey circles), Chl_{Canopy} (green circles) and SIF_{total} (brown circles) at the four soybean field sites: (a, e, i) BR3, (b, f, j) NE2, (c, g, k) NE3, and (d, h, l) UIUC. Filled circles are sunny days and open circles are cloudy days. The red, blue, grey, green, and brown dashed lines are the mean fitted lines for daytime mean far-red SIF, GPP, APAR, Chl_{Canopy} and SIF_{total} over sunny days, respectively. Time is shown as day of year (DOY). DOY of far-red SIF peak, GPP peak, APAR peak, Chl_{Canopy} peak and SIF_{total} peak are represented by the red, blue, grey, green and brown solid lines, respectively. The peak DOYs as well as the DOY difference between GPP and far-red SIF, and between Chl_{Canopy} and APAR are shown as texts. (For interpretation of the references to colour in this figure legend, the reader is referred to the web version of this article.)

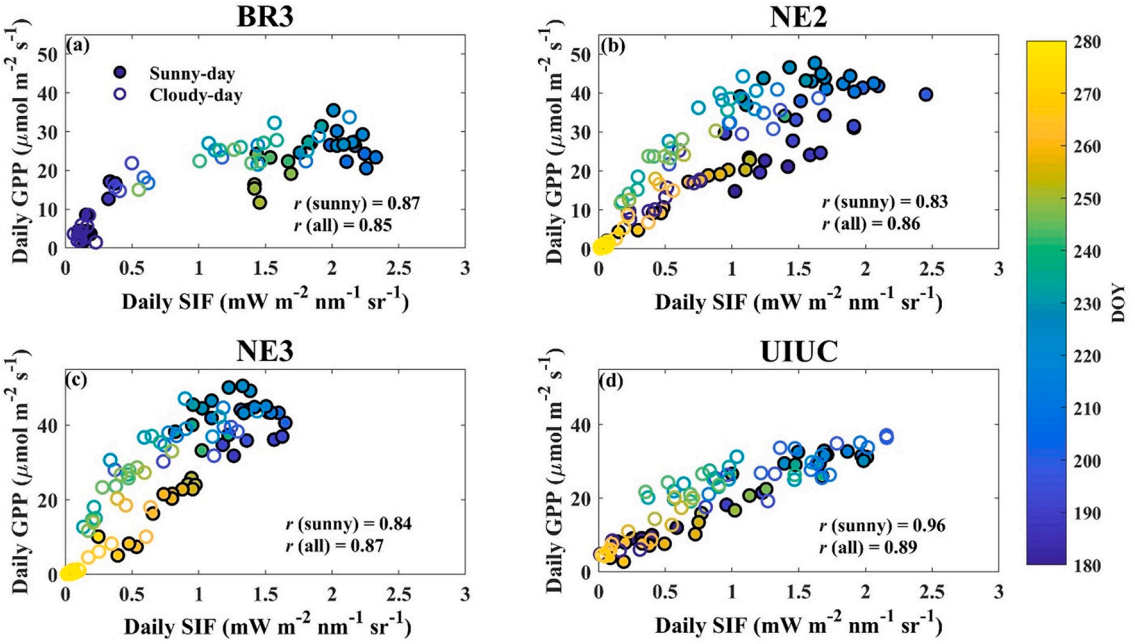

Fig. 3. Relationship between daytime mean far-red SIF and GPP at the four soybean sites: (a) BR3, (b) NE2, (c) NE3, and (d) UIUC. Filled circles are sunny days and open circles are cloudy days. Colormap represents day of year (DOY). The Pearson correlation coefficient (*r*) between far-red SIF and GPP on sunny days and all days are shown as texts. (For interpretation of the references to colour in this figure legend, the reader is referred to the web version of this article.)

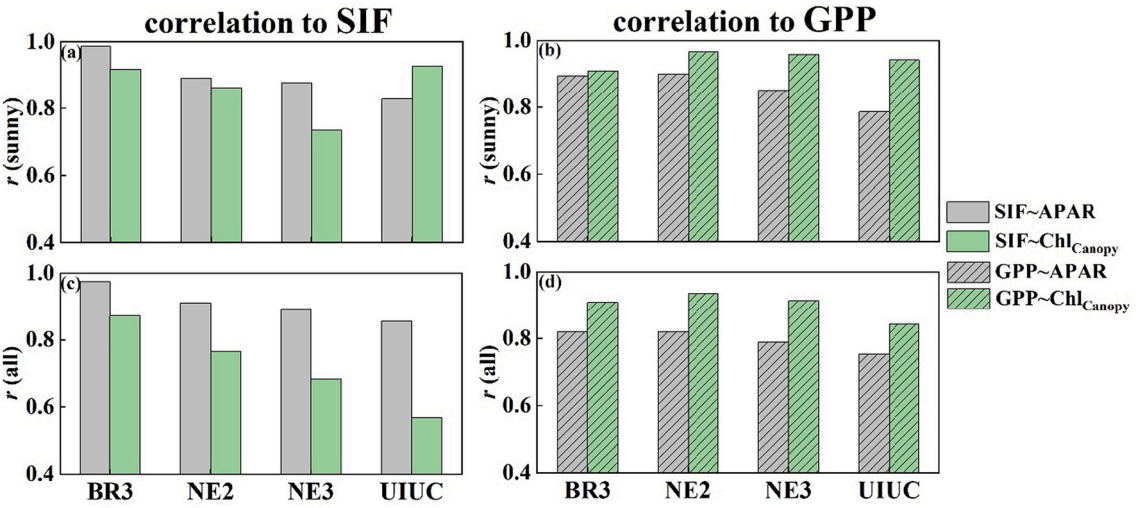

Fig. 4. Pearson correlation coefficient (*r*) between far-red SIF and APAR (a, b) (grey bar), between far-red SIF and Chl_{Canopy} (a, b) (green bar), between GPP and APAR (b, d) (grey dashed bar) and between GPP and Chl_{Canopy} (b, d) (green dashed bar) on sunny days (top rows) and all days (bottom rows) at the four soybean sites: BR3, NE2, NE3 and UIUC. All data used are daytime mean values. (For interpretation of the references to colour in this figure legend, the reader is referred to the web version of this article.)

showed relatively close peak times in Champaign County in 2019 (APAR: DOY 223, Chl_{Canopy}: DOY 232). In general, satellite data supported findings from tower data. Due to the larger difference in peak timing of far-red SIF and GPP in Saunders County, the relationship between far-red SIF and GPP in Saunders County ($r = 0.90$) was weaker than that in Champaign County ($r = 0.99$) (Fig. S8).

3.4. Seasonal variation of far-red SIF, GPP, APAR, and Chl_{Canopy} from SCOPE estimations

Seasonal peak timing difference between far-red SIF and GPP were observed from SCOPE estimations at the NE2 and NE3 sites (Fig. 6a and b), consistent with that from tower data (Fig. 2b-c). APAR and Chl_{Canopy} also showed similar peak timing difference as far-red SIF and GPP (Fig. 6d and e), consistent with that from tower data as well (Fig. 2f-g). Furthermore, the peak dates of far-red SIF (DOY 206 for NE2 NE3) were close to those of APAR (DOY 204 for NE2 and NE3), whereas the peak dates of GPP (DOY 220 for NE2 and NE3) were close to those of Chl_{Canopy} (DOY 222 for NE2 and DOY 219 for NE3). In addition, SCOPE SIF_{total} from all leaves showed similar peaks as far-red SIF (Fig. 6g and h). Similar to tower data, the peak timing dates of far-red SIF and GPP (Fig. 6c), and that of APAR and Chl_{Canopy} (Fig. 6f) at the UIUC site were relatively similar. Overall, SCOPE estimations supported findings from tower data, largely due to the agreements between SCOPE-estimated far-

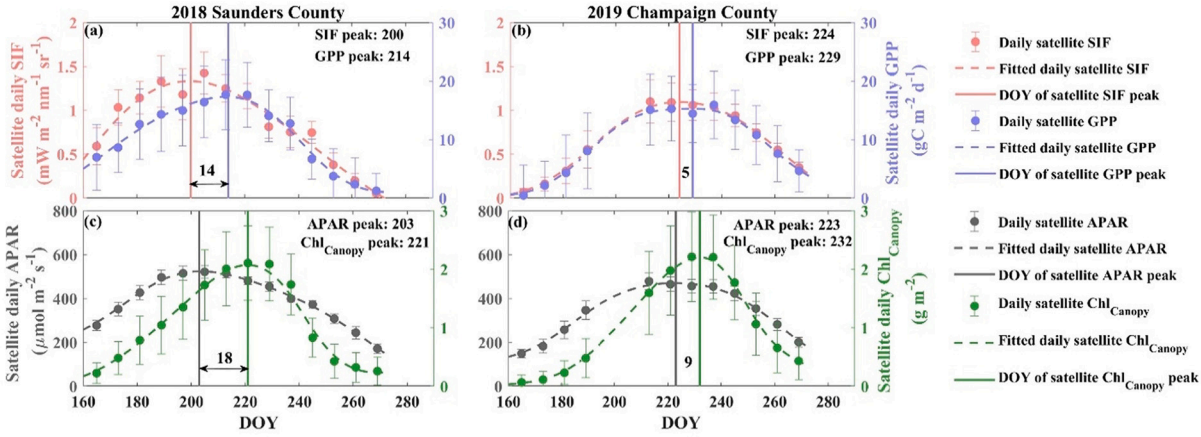

Fig. 5. Satellite-based seasonal variations of daily TROPOMI far-red SIF (red circles), Sentinel-2 derived GPP (blue circles), MODIS APAR (grey circles) and Sentinel-2 estimated Chl_{Canopy} (green circles) at two counties: (a) (c) 2018 Saunders County where the NE2 and NE3 sites are located, (b) (d) 2019 Champaign County where the UIUC site is located. The filled circles and error bars indicate county means and standard deviations, respectively. The red, blue, grey and green dashed lines are the mean fitted lines for satellite-based daily mean far-red SIF, GPP, APAR and Chl_{Canopy}, respectively. Time is shown as day of year (DOY). DOY of satellite-based daily far-red SIF, GPP, APAR and Chl_{Canopy} peak are represented by the red, blue, grey and green solid lines, respectively, and their peak DOYs as well as the DOY difference between GPP and far-red SIF peak, and the difference between Chl_{Canopy} and APAR peak are shown as texts. (For interpretation of the references to colour in this figure legend, the reader is referred to the web version of this article.)

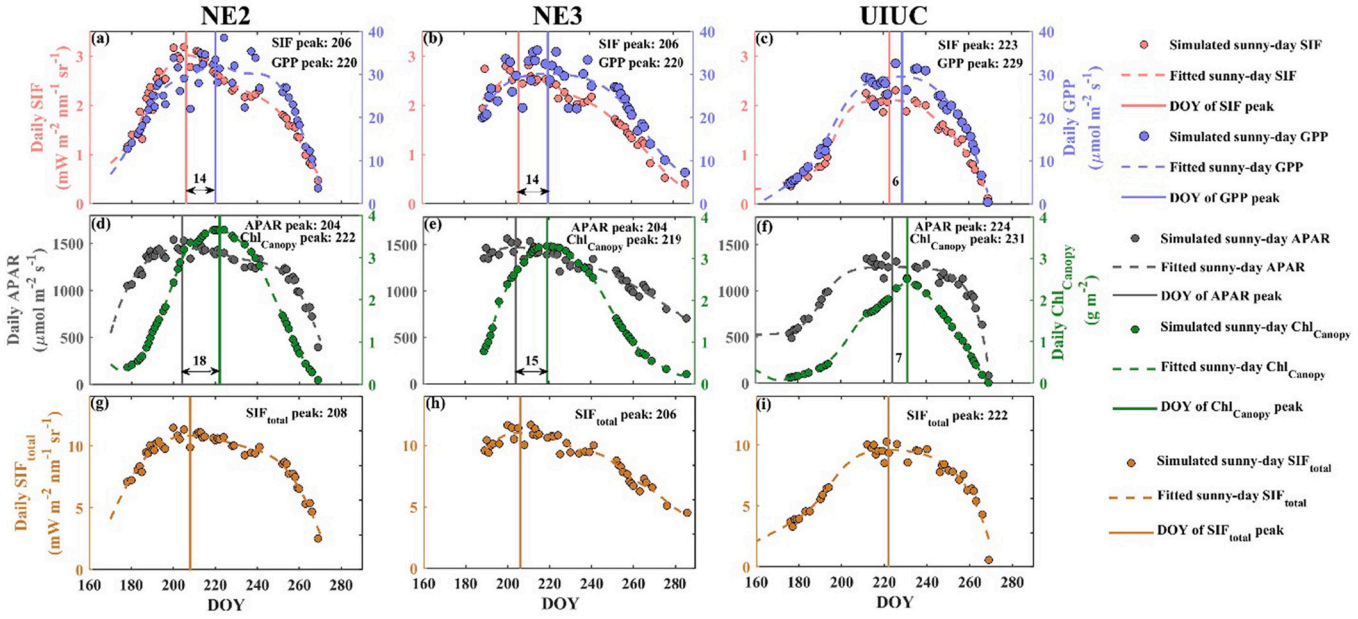

Fig. 6. SCOPE estimated seasonal variation of sunny-day mean far-red SIF (red circles), GPP (blue circles), APAR (grey circles), Chl_{Canopy} (green circles), SIF_{total} from all leaves (brown circles) emitted by all leaves at three sites: (a)(d)(g)NE2 site (b)(e)(h) NE3 site, (c)(f)(i) UIUC site. The red, blue, grey, green, and brown dashed lines are the mean fitted lines for simulated daily mean far-red SIF, GPP, APAR, Chl_{Canopy} and SIF_{total}, respectively. Time is shown as day of year (DOY). DOY of simulated daily far-red SIF, GPP, APAR, Chl_{Canopy} and SIF_{total} peak are represented by the red, blue, grey, green and brown solid lines, respectively, and their peak DOYs as well as the DOY difference between GPP and far-red SIF peak, the difference between Chl_{Canopy} and APAR peak and the difference between GPP and SIF_{total} peak are shown as texts. (For interpretation of the references to colour in this figure legend, the reader is referred to the web version of this article.)

red SIF, GPP, APAR, and Chl_{Canopy} and tower data (Fig. C1).

3.5. *Relationships between the peak timing of far-red SIF, GPP, APAR and Chl_{Canopy} from observations and SCOPE estimations*

When combining tower data, satellite data and SCOPE estimations, the peak date of far-red SIF and the peak date of APAR were significantly positively correlated (Fig. 7a, $r = 0.97$, p-value<0.01), and the peak date of GPP was strongly correlated with that of Chl_{Canopy} (Fig. 7b, $r = 0.87$, p-value<0.01). Across all the sites and counties from both observations and model estimations, the peak DOY difference between far-red SIF and APAR was small with maximum 4 days, and the peak DOY difference between GPP and Chl_{Canopy} was also smaller (maximum 7 days compared to that between GPP and APAR (maximum 16 days) (Fig. 7c). These results further demonstrated that overall, far-red SIF peaked at a similar time as APAR and GPP peaked similarly to Chl_{Canopy}. far-red SIF and GPP would peak at the similar time if APAR and Chl_{Canopy} peaked at the similar time, such as the UIUC site and the Champaign County.

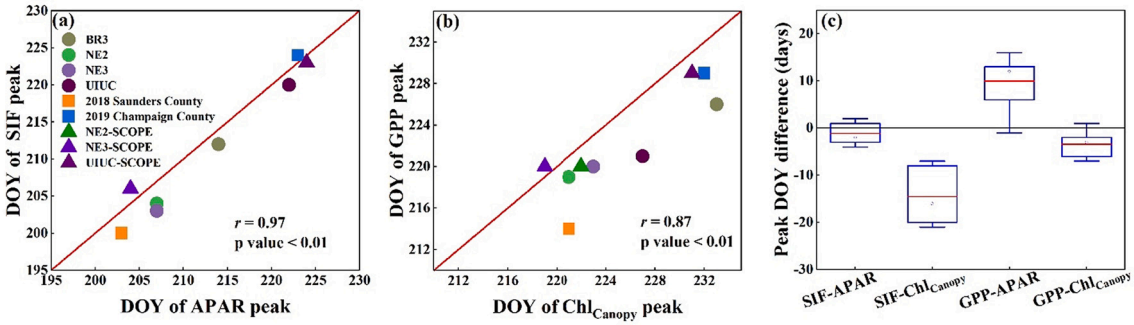

Fig. 7. Relationships between DOY of far-red SIF, GPP, APAR and Chl_{Canopy} peaks from tower data, satellite data and SCOPE estimations. (a) The scatterplot between DOY of APAR peak and DOY of far-red SIF peak; (b) The scatterplot between DOY of Chl_{Canopy} peak and DOY of GPP peak; (c) Boxplot of the peak DOY difference between far-red SIF and APAR, between far-red SIF and Chl_{Canopy}, between GPP and APAR, and between GPP and Chl_{Canopy}. Red line in (a) and (b) is the 1:1 line. Pearson *r* and p-value are shown. (For interpretation of the references to colour in this figure legend, the reader is referred to the web version of this article.)

3.6. The effect of LAI, Chl_{Leaf} and LAD on the seasonal variations of far-red SIF and GPP

Since APAR was strongly affected by LAI, LAD and Chl_{Leaf}, and Chl_{Canopy} was the product of LAI and Chl_{Leaf}, LAI, Chl_{Leaf} and LAD were analyzed at three sites: NE2, NE3 and UIUC. BR3 was not analyzed due to the lack of LAI data. We found three differences between the two NE sites where different seasonal peak timing of far-red SIF and GPP were observed and the UIUC site where no far-red SIF ~ GPP mismatch was observed. First, an earlier peak of LAI and later peak of Chl_{Leaf} was found at the two NE sites (Fig. 8a-b) while LAI and Chl_{Leaf} reached peak at the similar time at the UIUC site (Fig. 8c). Second, APAR reached the peak when LAI reached around 4 m^2 m^{-2}, and this date at the two NE sites was much earlier and further to the peak of Chl_{Leaf} compared to that at the UIUC site. Third, average leaf angle (ALA) at two NE sites were overall lower than that at the UIUC site (Fig. 8d).

SCOPE model simulations implied the findings from tower data that the peak DOY difference between Chl_{Leaf} and LAI, the seasonal shape of LAI, and the magnitude of ALA were potential factors for the far-red SIF ~ GPP mismatch (Fig. 9). First, peak DOY difference of Chl_{Leaf} and LAI is positively correlated with that of GPP and far-red SIF (Fig. 9a), and the absolute peak DOY difference of Chl_{Leaf} and LAI is negatively correlated with the correlation between GPP and far-red SIF (Fig. 9b). Second, a broad LAI shape (i.e., the date when LAI reached 4 m^2 m^{-2} was far away from the peak date) could exacerbate the peak timing difference of far-red SIF and GPP when the peak timing difference of Chl_{Leaf} and LAI were large (e.g., ≥ 40 days). Third, horizontal leaves (e.g., Planophile LAD) further caused larger far-red SIF ~ GPP difference than random leaves (e.g., Spherical LAD) and vertical leaves (e.g., Erectophile LAD).

Therefore, the later peak of Chl_{Leaf} compared to LAI, overall more horizontal leaves and the broader LAI seasonal shape contributed to the different seasonal peak timing of far-red SIF and GPP at the two NE sites.

4. Discussion

4.1. Mechanism of the seasonal peak timing difference between far-red SIF and GPP in soybean

In this study, we investigated the seasonal peaks of far-red SIF and GPP in soybean from tower data, county-level satellite data and site-level model estimations. We found that at three of four soybean fields, far-red SIF reaches its seasonal maximum prior to peak GPP, with peak date difference ranging from 14 to 17 days. Consistent with our hypotheses, we found that the seasonal peak timing of far-red SIF is similar

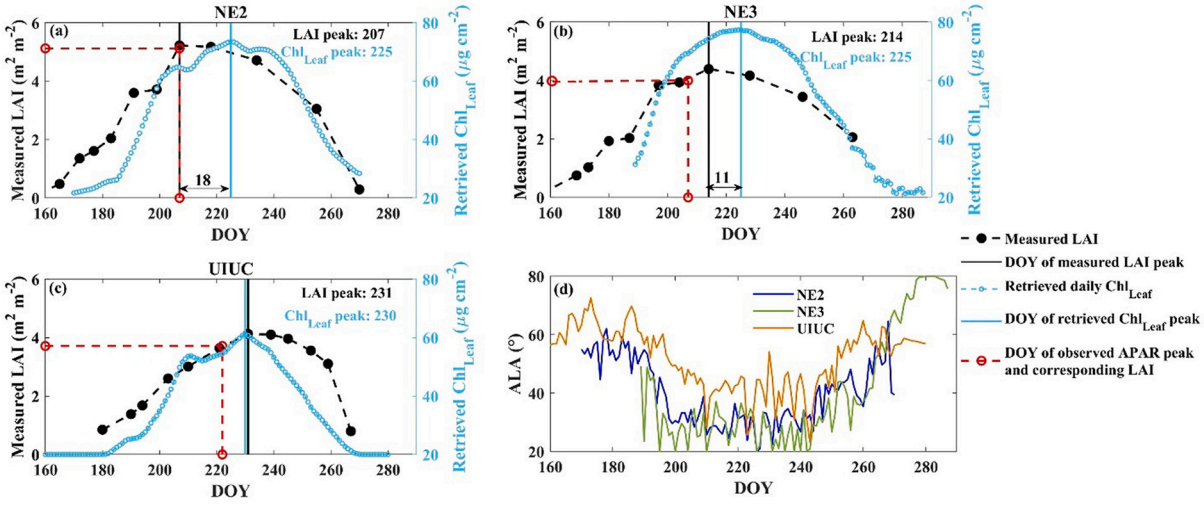

Fig. 8. Variations of leaf area index (LAI; black circles), leaf chlorophyll content (Chl_{Leaf}; blue circles) at three soybean sites: (a) NE2, (b) NE3 and (c) UIUC, and (d) The seasonal variation of retrieved daily average leaf angle (ALA) at the NE2, NE3 and UIUC site. Black and blue solid lines indicate the DOYs of LAI peak and Chl_{Leaf} peak, respectively. The peak DOYs of LAI and Chl_{Leaf} and the difference between Chl_{Leaf} and LAI peak are shown as texts. The red dashed lines indicate the DOY of APAR peak and the corresponding LAI value. (For interpretation of the references to colour in this figure legend, the reader is referred to the web version of this article.)

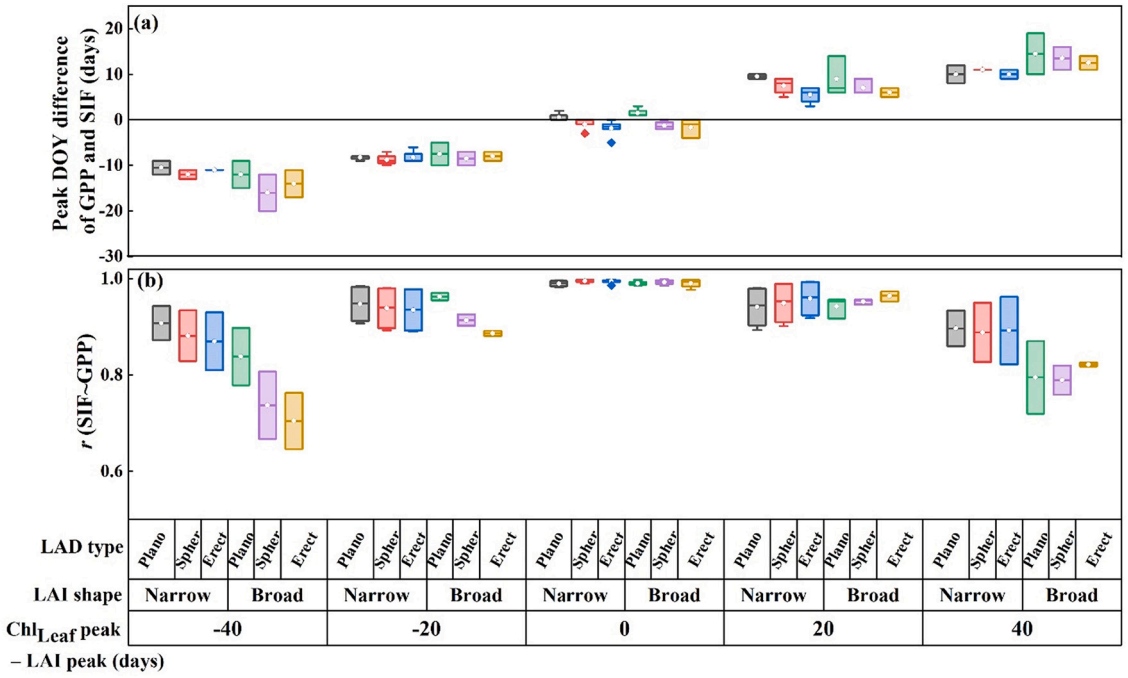

Fig. 9. The effect of LAI, Chl_{Leaf} and LAD on the relationship between far-red SIF and GPP from SCOPE simulations. (a) the peak DOY difference of simulated far-red SIF and GPP and (b) the Pearson correlation coefficient (r) between simulated daily far-red SIF and GPP under different peak DOY differences of Chl_{Leaf} and LAI (−40 days, −20 days, 0 day, 20 days and 40 days), different LAI seasonal shapes (narrow, broad) and different LAD types (Planophile (Plano), Spherical (Spher) and Erecophile (Erect)). (For interpretation of the references to colour in this figure legend, the reader is referred to the web version of this article.)

to the seasonal peak timing of APAR, and the seasonal peak timing of GPP is similar to the seasonal peak timing of Chl_{Canopy}. As SIF_{total} still shows a mismatch in the seasonal peak timing compared to GPP, we can exclude the effect of canopy scattering as captured by the escape fraction (f_{esc}) and explain the peak timing difference between far-red SIF and GPP.

The seasonal peak timing of far-red SIF, a product of the light reactions of photosynthesis, is primarily driven by APAR, whereas the

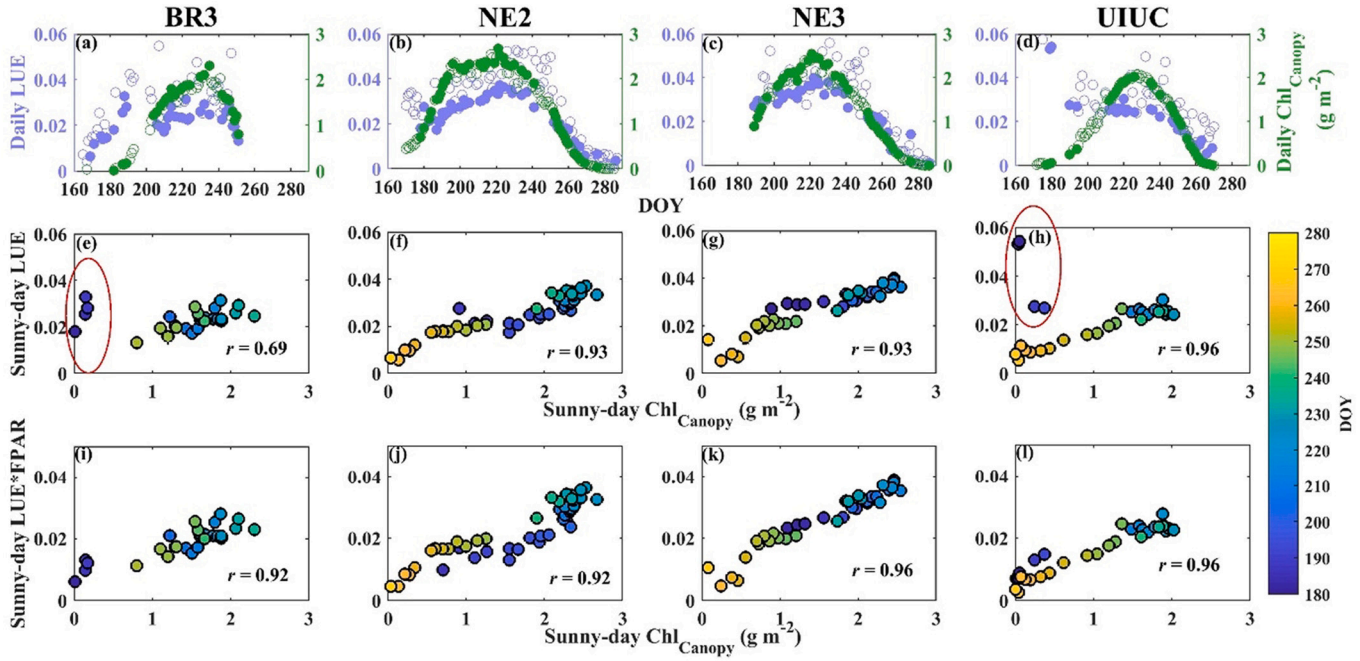

Fig. 10. Relationship between Chl_{Canopy} and LUE from tower observations at the four soybean sites. Seasonal variations of daily LUE (blue circles) and Chl_{Canopy} (green circles) at the (a) BR3, (b) NE2, (c) NE3 and (d) UIUC site. Filled circles are sunny days and open circles are cloudy days. The relationship between sunny-day LUE and sunny-day Chl_{Canopy} at the (e) BR3, (f) NE2, (g) NE3 and (h) UIUC. The relationship between the product of sunny-day LUE and FPAR (LUE*FPAR) and sunny-day Chl_{Canopy} at the (i) BR3, (j) NE2, (k) NE3 and (l) UIUC. Colormap represents day of year (DOY). The Pearson correlation coefficients (r) between sunny-day LUE and Chl_{Canopy} and between sunny-day LUE*FPAR and Chl_{Canopy} are shown as texts. For (e) BR3 and (h) UIUC sites, early growing season data (circled by the red ellipse) are excluded for the r calculation. (For interpretation of the references to colour in this figure legend, the reader is referred to the web version of this article.)

seasonal peak timing of GPP is more dominated by Chl_{Canopy}. The dominant role of APAR on the far-red SIF signal in crops has been reported in many studies (Dechant et al., 2020; Miao et al., 2018, 2020; Yang et al., 2018a). Thus, the similar seasonal peak dates of soybean far-red SIF and APAR observed in this study are expected. GPP, however, is not only affected by APAR but also LUE. LUE cannot be directly measured and many proxies have been used to parameterize LUE such as photochemical reflectance index (Gamon et al., 1997). Among these proxies, Chl_{Canopy} has been shown to be important in LUE and GPP estimation, and many studies have found significant positive correlations between LUE and Chl_{Canopy} as well as between GPP and Chl_{Canopy} at seasonal scale across various ecosystems (Croft et al., 2015; Wu et al., 2009, 2012). The strong relationship between GPP and Chl_{Canopy} is also confirmed in our soybean sites (Fig. 4; Fig. B1).

The strong GPP- Chl_{Canopy} correlations can possibly be explained for three reasons. First, LAI has a large impact on LUE because it determines the partitioning of light-saturated (sunlit) and light-limited (shaded) canopies (Medlyn, 1998). Second, Chl_{Leaf} is strongly correlated with Rubisco content and has been used to estimate V_{cmax} at the seasonal scale across various ecosystems (Croft et al., 2017; Houborg et al., 2015b; Lu et al., 2020; Qian et al., 2021), and this strong correlation is also confirmed from tower data at a soybean site (Fig. S9). This tight link between Chl_{Leaf} and V_{cmax} also explains the important role of Chl_{Canopy} in LUE. When the early growing season during which LUE is high due to low FPAR is excluded, sunny-day LUE and Chl_{Canopy} is strongly correlated at our four soybean sites ($r = 0.69$–0.96) (Fig. 10e-h). The positive relationship between LUE and Chl_{Canopy} leads to a further increase of LUE when APAR starts to decrease (Fig. 10a-d), which results in the later peak of GPP compared to APAR. In addition to LUE, Chl_{Canopy} also accounts for the fraction of light capture (FPAR) information since both LAI and Chl_{Leaf} are important for light absorption (Gitelson et al., 2014). This is particularly important for the early growing season when FPAR is low. After taking FPAR into account, the correlation between Chl_{Canopy} and the product of LUE and FPAR (LUE*FPAR) is strong across the whole growing season ($r = 0.92$–0.96) (Fig. 10i-l). This strong correlation between Chl_{Canopy} and LUE, as well as between Chl_{Canopy} and LUE*FPAR, is also supported by the SCOPE model estimates (Fig. S10). While Chl_{Canopy} does not contain radiation (PAR) information which is another important factor for GPP, this study focuses on the seasonal scale at which the role of PAR is less important (Wu et al., 2020). Incorporating PAR information into Chl_{Canopy}, i.e., the product of Chl_{Canopy} and PAR (Chl_{Canopy}*PAR), does not change the seasonal pattern as well as the peak date of Chl_{Canopy} itself. The correlation between Chl_{Canopy}*PAR and GPP is similar as that between Chl_{Canopy} and GPP at daily scale (Fig. D1). The above explanations indicate that the similar seasonal peak timing of GPP and Chl_{Canopy} is reasonable. This phenomenon has also been reported in a temperate forest (Croft et al., 2015). Earlier peaks of soybean APAR compared to GPP have also been shown in some soybean fields (Gitelson et al., 2015), which further demonstrates the important role of Chl_{Canopy} in soybean GPP estimation at seasonal scale. We note that the seasonal trajectory of Chl_{Canopy} has a sharper peak compared to the APAR seasonality, which might increase some uncertainties for APAR peak detection compared to Chl_{Canopy}. However, from their seasonal trajectories, we can visually observe that far-red SIF and APAR reach seasonal maximum at a similar time and that GPP and Chl_{Canopy} reach seasonal maximum at a similar time (Fig. 2). Therefore, the seasonal peak timing difference between far-red SIF and GPP is strongly dependent on the seasonal peak timing of APAR and Chl_{Canopy}.

Two growth characteristics of soybean can justify the seasonal mismatch between APAR and Chl_{Canopy}, and consequently between far-red SIF and GPP. First, soybean is characterized by horizontal leaves which generally have higher light interception compared to vertical leaves (Nobel et al., 1993). Second, soybean tends to have a broad LAI seasonal shape, i.e., its LAI reaches a high value (e.g., 3–4 m^2 m^{-2}) quickly but then takes long time to reach its peak value (usually >5 m^2 m^{-2}). When soybean LAI reaches 3–4, FPAR becomes saturated (Thenkabail et al., 2011). Because PAR decreases during the peak growing season (July–September), APAR reaches its peak once FPAR is saturated. However, LAI still increased gradually for 5–15 days to reach its maximum at the two NE2 sites. This further increase of LAI after FPAR saturation and the further increase of Chl_{Leaf} after LAI reaching its maximum (Houborg et al., 2015a) resulted in a later peak of Chl_{Canopy} compared to APAR at the two NE2 sites (Fig. 8). At the UIUC site, however, because of the late planting due to flooding in spring and early summer of 2019 (Yin et al., 2020), a lower magnitude of LAI, a later peak of APAR, and a similar peak timings of LAI and Chl_{Leaf} was observed (Fig. 8), which yielded a similar peak timing for APAR and Chl_{Canopy}, and consequently for far-red SIF and GPP. Different seasonal peak timing between far-red SIF and GPP has a higher likelihood to be observed in dense canopies with high maximum LAI, broad LAI seasonal shape, more horizontal leaves and different peak timing of LAI and Chl_{Leaf}. Although our study focuses on soybean, the framework about the relationship between far-red SIF, GPP, APAR and Chl_{Canopy} can be potentially applied to other ecosystems to investigate whether the peak mismatch between far-red SIF and GPP is common or rather unique to soybean. For corn grown at our NE3 and UIUC sites from different years, we did not find a notable difference in peak timing of far-red SIF and GPP since APAR and Chl_{Canopy} reach their peak at a similar time at these two sites (Fig. S11). Examining the potential existence of peak mismatches between far-red SIF and GPP, as well as their relationships to APAR and Chl_{Canopy}, in other crops and natural ecosystems is of considerable interest but goes beyond the scope of this study. It is worth mentioning that the sites in this study are not severely stressed, indicated by the normal soil water content at the NE2, NE3 and UIUC site (Fig. S12). Previous studies have shown that stress can considerably affect the linearity of the far-red SIF-GPP relationship (Martini et al., 2021; Wieneke et al., 2018; Wohlfahrt et al., 2018), which suggests that seasonal patterns of far-red SIF and GPP could be considerably affected by stress. Future studies could apply the analyses we conducted to larger far-red SIF data collections such as ChinaSpec (Zhang et al., 2021) which could provide insights across ecosystems and climatic conditions.

4.2. Sources of uncertainties in this study

We acknowledge that there are multiple sources of uncertainties in this study, mainly coming from far-red SIF retrieval methods, the footprint correction of observed nadir-view far-red SIF, sunny-day threshold definition, the different ways of calculation of FPAR and Chl_{Canopy}, and the unmixing of TROPOMI far-red SIF into far-red SIF of different land cover types. We will provide a detailed discussion here, and also provide justification that these uncertainties do not affect the general conclusion that we drew.

We are aware that the retrieved far-red SIF from different sites has some uncertainties. First, there are differences between far-red SIF observations from multi-angle view (PhotoSpec at BR3 site) and nadir view settings (Fluospec2 at other three sites). Second, far-red SIF retrieval can introduce some uncertainties, largely due to its small signal compared to the reflected sunlight background (Damm et al., 2011; Meroni et al., 2009). Third, different retrieval methods are used at the BR3 site and other three sites, but a recent study has shown that different retrieval methods have little impact on sunny-day far-red SIF (Chang et al., 2020). We also note that far-red SIF magnitude differs in different sites, but this does not affect the seasonality. The different magnitude between BR3 and other three sites is likely due to different instrumentation setup and different far-red SIF retrieval algorithms (Chang et al., 2020; Marrs et al., 2021). The higher far-red SIF at the NE2 site than that at the NE3 site but similar GPP magnitude at these two sites is resulted from high f_{esc} shown at the NE2 site (Fig. S6), due to higher LAI (Yang and van der Tol, 2018), which leads to a higher proportion of SIF_{total} to be observed by the sensor. After accounting for the f_{esc} effect, SIF_{total} at the two sites are quite similar (Fig. 2). However, with these differences existing, we still observe a consistent pattern across sites, i.e., far-red SIF better

follows APAR and GPP better follows Chl_{Canopy} regarding the seasonal peak timing. Additionally, the SCOPE model results which are unrelated to far-red SIF retrieval uncertainty are consistent with tower results, which suggests that the uncertainties caused by far-red SIF retrievals do not affect our main findings.

Two assumptions were used in the footprint correction of observed far-red SIF. First, we did not consider the PAR variation within the GPP footprint and far-red SIF observation area. This assumption is valid under clear-sky conditions which are the major focus of this study (Jiang et al., 2020). Second, we did not consider the variation of the relationship between far-red SIF and NIRvP. A recent study has showed that when combing spatial and temporal scales, NIRvP can still explain around 80% of far-red SIF (Dechant et al., 2022; Kimm et al., 2021), indicating that using NIRvP to correct observed far-red SIF can capture the majority far-red SIF difference between the GPP footprint and far-red SIF observation area. Additionally, footprint correction did not strongly modify the seasonal patterns of far-red SIF, and both corrected and directly observed far-red SIF still shows an earlier peak than GPP at the two NE sites. We note that different sunny-day definitions affect the absolute seasonal peak DOY difference between far-red SIF and GPP (ranging from 12 to 19 days at the NE2 site, Fig. S13), but the earlier peak of far-red SIF compared to GPP is consistent across different sunny day thresholds.

It is worth noting that we used different FPAR at different sites. At the BR3 site, NDVI is used as a proxy of FPAR due to the absence of direct measurements. At other three sites, direct measured FPAR that captures the light absorbed by all leaves ($FPAR_{total}$) are used. Previous studies suggest that FPAR from all green leaves ($FPAR_{green}$) better captures the light absorption by chlorophylls (Gitelson and Gamon, 2015), but this dataset is only available at the two NE sites, preventing a consistent application at other sites. Using different FPAR calculations is expected to have an impact mainly during the senescence phase at the end of the growing season, however, in this study, we mainly focus on the seasonal peak of APAR rather than the end of growing season. Although NDVI at the NE2 site shows an earlier saturation date compared to $FPAR_{total}$ due to the irrigation effect, similar saturation time between NDVI and other $FPAR_{total}$ is shown at the NE3 site, which is also a rainfed site as the BR3 site. Thus, we would expect that at the BR3 site, using NDVI as the FPAR proxy can still capture the seasonal peak of APAR. Additionally, $FPAR_{total}$ and $FPAR_{green}$ at the two NE sites show the same starting saturation date, indicating that using $FPAR_{total}$ well captures the seasonal peak of APAR (Fig. S14). These results demonstrate that the different FPAR data used at the four sites do not affect the seasonal peaks of APAR, and therefore do not affect our findings on seasonal mismatches.

We also note that direct measurements of Chl_{Canopy} are absent in this study. Instead, we used the $CI_{rededge}$ calculated from canopy reflectance for the Chl_{Canopy} estimation. $CI_{rededge}$ mainly relates to the top canopy chlorophyll content rather than the total canopy chlorophyll content. However, Gitelson et al. (2006) has compared the total canopy chlorophyll content in the entire plant with the upper canopy chlorophyll content which is the product of LAI and Chl_{Leaf} from the upper canopy. Their results have shown that total chlorophyll content in the canopy can be accurately estimated using the upper canopy chlorophyll content which can be further well estimated by $CI_{rededge}$ (Gitelson et al., 2005). For the SCOPE model simulations, Chl_{Leaf} is retrieved from the PROSAIL model. Although PROSAIL has a horizontally-homogeneous canopy assumption without considering row effect or clumping effect, this approach has been widely used in many studies (Berger et al., 2018; Houborg et al., 2015a; Zhang et al., 2005). We acknowledge that the retrieved Chl_{Leaf} showed larger seasonal variations than measured Chl_{Leaf} (Houborg et al., 2015a), but in this study we focused more on the peak timing of Chl_{Leaf} and the pattern of later peak of Chl_{Leaf} than LAI at the two NE sites is consistent with the measurements (Houborg et al., 2015a). To further evaluate the $CI_{rededge}$-based Chl_{Canopy} estimate, $CI_{rededge}$ is calculated using SCOPE reflectance output. $CI_{rededge}$-based Chl_{Canopy} and the Chl_{Canopy} calculated as the product of LAI and Chl_{Leaf} ($LAI*Chl_{Leaf}$), are compared. Overall, there was a similar seasonal pattern and strong relationship between these two Chl_{Canopy} estimates with Pearson r ranging from 0.98 to 0.99 are observed at the NE2, NE3 and UIUC site (Fig. S15). Although $LAI*Chl_{Leaf}$-based Chl_{Canopy} is higher than $CI_{rededge}$-based Chl_{Canopy} and shows some nonlinearity which needs further investigation in the future study, this difference does not affect the seasonality which is the major focus of our study. Retrieved Chl_{Leaf} is also used for SCOPE input V_{cmax} estimation considering that Chl_{Leaf} and V_{cmax} are strongly correlated in both space and time (Croft et al., 2017; Houborg et al., 2015b; Lu et al., 2020). Our dataset from another soybean site further confirms their strong correlation at seasonal scale (Fig. S9). Furthermore, we conducted CO_2 response curve measurements at the NE2 site twice in 2018, and the result shows a higher V_{cmax} at 25° in August compared to July (Fig. S16), which is consistent with the retrieved Chl_{Leaf} pattern. Despite these uncertainties, the above evidence supports the credibility of our main findings.

Finally, the unmixing algorithm to derive soybean far-red SIF from TROPOMI landscape far-red SIF could have uncertainty. The uncertainly mainly lies in the assumption that far-red SIF yield of a specific land cover type (corn, soybean, forest or grass) is invariant within a certain area (e.g., a county). This is overall reasonable because local farmers generally have similar management practices (e.g., planting, fertilizing and weeding) in the study area. Moreover, within-county variability mainly causes uncertainty of far-red SIF unmixing with regard to spatial patterns, but less influences county-scale seasonal trajectories of corn and soybean far-red SIF which is the focus of this study.

4.3. Implications for GPP estimation

The ultimate motivation to study the relationships between SIF and GPP is to improve the remote estimation of GPP (Ryu et al., 2019). In this study, we found seasonal peak timing difference between SIF and GPP in some soybean fields. Clear seasonal hysteresis between SIF and GPP were observed at the sites where SIF reached seasonal maximum earlier than GPP, which degraded the SIF-GPP relationships and challenged the approach that solely uses SIF for the GPP estimation (Li and Xiao, 2019; Zhang et al., 2020b). SIF mainly emanates from light reactions of photosynthesis which have been reported in many previous studies (Dechant et al., 2020; He et al., 2020; Yang et al., 2021). SIF itself has limited capability to capture the seasonal variation of GPP at fine time scales when there is a seasonal peak timing difference between SIF and GPP, e.g., daily scale for soybean in this study. Escape ratio corrected SIF_{total} still shows a peak timing difference compared to GPP, demonstrating that currently corrected SIF_{total} still has limitations in improving the GPP estimation at seasonal scale. Escape ratio correction seems to result in more consistent SIF-GPP relationship across various ecosystems (Zhang et al., 2020b), but it cannot improve the temporal variation with regard to crop GPP estimations (Dechant et al., 2020; Zhang et al., 2019). There are two possible reasons: 1) Current escape ratio calculations still have large uncertainties which increases the uncertainty of SIF_{total}-GPP relationships; 2) Both SIF_{total} and observed SIF are product of light reactions of photosynthesis whereas GPP is composed of both light and carbon reactions (Magney et al., 2020).

The consistent seasonal peak timing between Chl_{Canopy} and GPP and the strong relationship between GPP and Chl_{Canopy} (Pearson $r > 0.9$ across all sites) demonstrates that Chl_{Canopy} is important for GPP estimation at seasonal scale. The improvement of GPP estimation using Chl_{Canopy} compared to using SIF is mainly due to the strong link between Chl_{Leaf} and V_{cmax}. V_{cmax} is substantially important for GPP and it is a key physiological control parameter for photosynthesis estimations using terrestrial biosphere models (Farquhar et al., 1980). SIF is generally less sensitive to the V_{cmax} variation compared to GPP (Frankenberg and Berry, 2018; Zhang et al., 2016). Although several studies have used SIF to constrain the V_{cmax} estimation using process-based models, the performance varies case by case (Koffi et al., 2015; Pacheco-Labrador et al.,

2019; Verma et al., 2017; Zhang et al., 2014). Tower measurements indeed find that V_{cmax} and SIF are correlated in a rice paddy, but this correlation is relatively weak and varies with growth stages (Li et al., 2020). Chl_{Leaf} has been shown to be a strong proxy of V_{cmax} in both space and time (Croft et al., 2017; Lu et al., 2020; Qian et al., 2021). It is worth mentioning that compared to SIF, Chl_{Canopy} does not carry the radiation information which is important for sub-daily GPP (Wu et al., 2020). Previous studies have proposed that the model based on the product of incoming PAR and Chl_{Canopy} works well in the GPP estimations for corn and soybean GPP at sub-daily scale in the U.S. Corn Belt (Gitelson et al., 2012; Peng and Gitelson, 2012). Considering that SIF still has its unique physiological information compared to other vegetation indices (Porcar-Castell et al., 2014), especially under stress conditions (Qiu et al., 2020; Song et al., 2018), combining SIF and Chl_{Canopy} could potentially improve the GPP estimation.

In terms of large-scale GPP estimation using satellite observations, the temporal resolution of currently available grided satellite SIF product is coarse, e.g., $>$ 1 week (Mohammed et al., 2019). In this case, the seasonal peak timing difference between SIF and GPP may not be captured. In this study, we used downscaled 8-day satellite SIF and were able to detect this difference in soybean, which demonstrates the importance of fine spatiotemporal satellite SIF products (Duveiller et al., 2019). Future SIF products from geostationary missions such as GeoCarb (Moore et al., 2018) and TEMPO (Zoogman et al., 2017) could provide daily and sub-daily observations, at which the impact of seasonal peak timing difference between SIF and GPP would be more important when solely using SIF for GPP estimation. In this case, incorporating chlorophyll information might be necessary for some crops and ecosystems. Many studies have successfully retrieved Chl_{Canopy} and Chl_{Leaf} using Sentinel-2 and Sentinel-3 observations (Clevers et al., 2017; Upreti et al., 2019; Weiss and Baret, 2016), which provides a potential to combine SIF and Chl_{Canopy} or Chl_{Leaf} for large-scale sub-daily to daily GPP estimations.

5. Conclusions

We investigated the seasonal trajectories of far-red SIF and GPP in soybean using site-level tower data, county-level satellite data and site-level model simulations. We found different seasonal peak timing of far-red SIF and GPP in three of four soybean fields, i.e., far-red SIF reached seasonal maximum 14–17 days earlier than GPP. This was mainly due to the fact that the seasonal peak timing of far-red SIF was more dominated by the seasonal peak timing of APAR, whereas the seasonal peak timing of GPP was similar as the seasonal peak timing of Chl_{Canopy}. The seasonal peak timing difference of far-red SIF and GPP was therefore determined by the timing of APAR and Chl_{Canopy}, which was further controlled by the seasonal pattern of LAI, LAD and Chl_{Leaf}. The broad LAI seasonal shape, high maximum LAI and more horizontal leaves in soybean fields caused an earlier FPAR saturation, and thus earlier peak timing of APAR and far-red SIF. The further increase of LAI after FPAR saturation and increase of Chl_{Leaf} after LAI peak resulted in a later seasonal peak of Chl_{Canopy} and GPP. This peak timing difference between far-red SIF and GPP challenges the approach to solely use far-red SIF for the GPP estimation, and combining far-red SIF and Chl_{Canopy} could potentially improve the GPP estimation. Our findings focus on the seasonal trajectory of far-red SIF and GPP and highlight the importance of chlorophyll content in GPP estimation.

Appendix A. Details of the SCOPE modeling process in this study

CRediT authorship contribution statement

Genghong Wu: Conceptualization, Methodology, Validation, Formal analysis, Investigation, Data curation, Writing – original draft, Writing – review & editing, Visualization. **Chongya Jiang:** Conceptualization, Methodology, Validation, Formal analysis, Investigation, Data curation, Writing – review & editing, Visualization. **Hyungsuk Kimm:** Conceptualization, Methodology, Data curation, Investigation, Writing – review & editing. **Sheng Wang:** Conceptualization, Investigation, Writing – review & editing. **Carl Bernacchi:** Methodology, Investigation, Writing – review & editing. **Caitlin E. Moore:** Methodology, Data curation, Investigation, Writing – review & editing. **Andy Suyker:** Methodology, Data curation, Investigation, Writing – review & editing. **Xi Yang:** Conceptualization, Methodology, Investigation, Writing – review & editing. **Troy Magney:** Conceptualization, Methodology, Data curation, Investigation, Writing – review & editing. **Christian Frankenberg:** Methodology, Investigation, Writing – review & editing. **Youngryel Ryu:** Conceptualization, Methodology, Investigation, Writing – review & editing. **Benjamin Dechant:** Conceptualization, Methodology, Investigation, Writing – review & editing. **Kaiyu Guan:** Conceptualization, Funding acquisition, Investigation, Project administration, Resources, Supervision, Writing – review & editing.

Declaration of Competing Interest

The authors declare that they have no known competing financial interests or personal relationships that could have appeared to influence the work reported in this paper.

Acknowledgement

GW and KG are supported by NASA Future Investigators in NASA Earth and Space Science and Technology (FINESST) Program. GW, KG, and HK, acknowledge the support from NASA New Investigator Award and NASA Carbon Monitoring System program managed by the NASA Terrestrial Ecology Program. We thank Guofang Miao for the Fluospec2 system maintenance and data collection at the NE2 and NE3 sites. We thank M. Pilar Cendrero-Mateo for sharing the iFLD code for SIF retrieval.

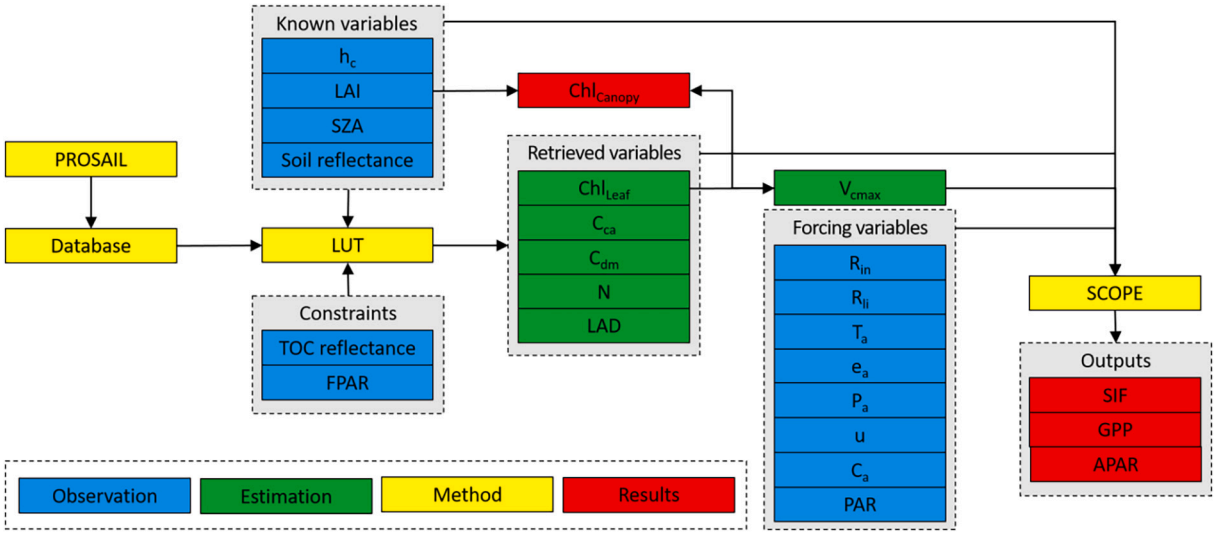

Fig. A1. Schematic diagram of the process-based modeling for the estimations of SIF, GPP, APAR and Chl_{Canopy}. hc: canopy height. LAI: leaf area index. SZA: solar zenith angle. FPAR: fraction of absorbed photosynthetically active radiation. Chl_{Leaf}: leaf chlorophyll content. C_{ca}: leaf carotenoid content. C_{dm}: leaf dry matter content. N: leaf thickness parameter. LAD: leaf angle distribution. V_{cmax}: Rubisco maximum carboxylation rate. R_{in}: shortwave radiation. R_{li}: longwave radiation. T_a: air temperature. e_a: ambient water vapor. P_a: air pressure. u: wind speed. C_a: ambient CO_2 concentration. PAR: photosynthetically active radiation. A summary of SCOPE model parameters is listed in Table A1.

Table A1
Summary of SCOPE model parameters that are relevant to SIF and GPP simulations.

Parameter	Value	
	Real-world simulation	Scenario simulation
R_{in}	Observation	R_{TOA} × mean diurnal cycle of clear-day R_{in}/R_{TOA}, where R_{TOA} is a function of location and time.
R_{li}	Observation	Mean diurnal cycle of clear-day R_{li}
T_a	Observation	Mean diurnal cycle of clear-day T_a
e_a	Observation	Mean diurnal cycle of clear-day e_a
P_a	Observation	Mean diurnal cycle of clear-day P_a
u	Observation	Mean diurnal cycle of clear-day u
C_a	Observation	Mean diurnal cycle of clear-day C_a
PAR	Observation	Mean diurnal cycle of clear-day PAR
R_{soil}	Observation	Mean R_{soil} of the three sites
LAI (m^2 m^{-2})	Observation	$a_1 \times \exp.\{-[(DOY-b_1)/c_1]^2\}$*, where $a_1 = 4.5$, $b_1 = \{200, 220, 240\}$, $c_1 = \{30, 60\}$
h_c (m)	Observation	0.8
Chl_{Leaf} (μg cm^{-2})	Retrieved from R_{canopy} and FPAR	$a_2 \times \exp.\{-[(DOY-b_2)/c_2]^2\}$**, where $a_2 = 75$, $b_2 = \{200, 220, 240\}$, $c_2 = \{30, 60\}$
C_{ca} (μg cm^{-2})	Retrieved from R_{canopy} and FPAR	10
C_{dm} (g cm^{-2})	Retrieved from R_{canopy} and FPAR	0.005
N	Retrieved from R_{canopy} and FPAR	1.75
LAD	Retrieved from R_{canopy} and FPAR	Planophile; Erectophile
C_w (cm)	0.01	0.01
C_s	0	0
V_{cmax} (μmol m^{-2} s^{-1})	Chl_{Leaf} × 1.75–10.1	Chl_{Leaf} × 1.75–10.1
m	13.5	13.5
b_0	0	0
k_V	0	0
Rdparam	0.0089	0.0089
Tparam	[0.2, 0.3, 281, 308, 328]	[0.2, 0.3, 281, 308, 328]
SMC	0.25	0.25

* a_1: maximum LAI over the season; b_1: DOY when LAI reaches its peak; c_1: shape parameter of LAI seasonality. Larger c_1 indicates a broader LAI seasonal trajectory whereas smaller c_1 indicates a steeper LAI seasonal trajectory.

** a_2: maximum Chl_{Leaf} over the season; b_2: DOY when Chl_{Leaf} reaches its peak; c_2: shape parameter of Chl_{Leaf} seasonality. Larger c_2 indicates a broader Chl_{Leaf} seasonal trajectory whereas smaller c_2 indicates a steeper Chl_{Leaf} seasonal trajectory.

Table A2
Parameter values needed to establish the canopy reflectance database by PROSAIL. A total of 5180 databases was built, with LAI ranging from 0.1 to 7.0 at 0.1 interval and solar zenith angle ranging from 17 to 80 at 1 degree interval.

Parameters	Values
LAD (a.u.)	Planophile, Erectophile, Plagiophile, Extremophile, Spherical, Uniform
Chl_{Leaf} (μg cm^{-2})	20, 30, 40, 50, 60, 70, 80, 90, 100
C_{ar} (μg cm^{-2})	2.5, 5, 10, 15
C_m (g cm^{-2})	0.001, 0.005, 0.01, 0.015
N (a.u.)	1, 1.5, 2, 2.5
C_{brown} (a.u.)	0
C_w (cm)	0.01
Hotspot parameter (a.u.)	0.1
View zenith angle (°)	0
Azimuth angle (°)	0

Appendix B. Relationship of SIF, GPP, APAR and Chl_{Canopy} from tower observations

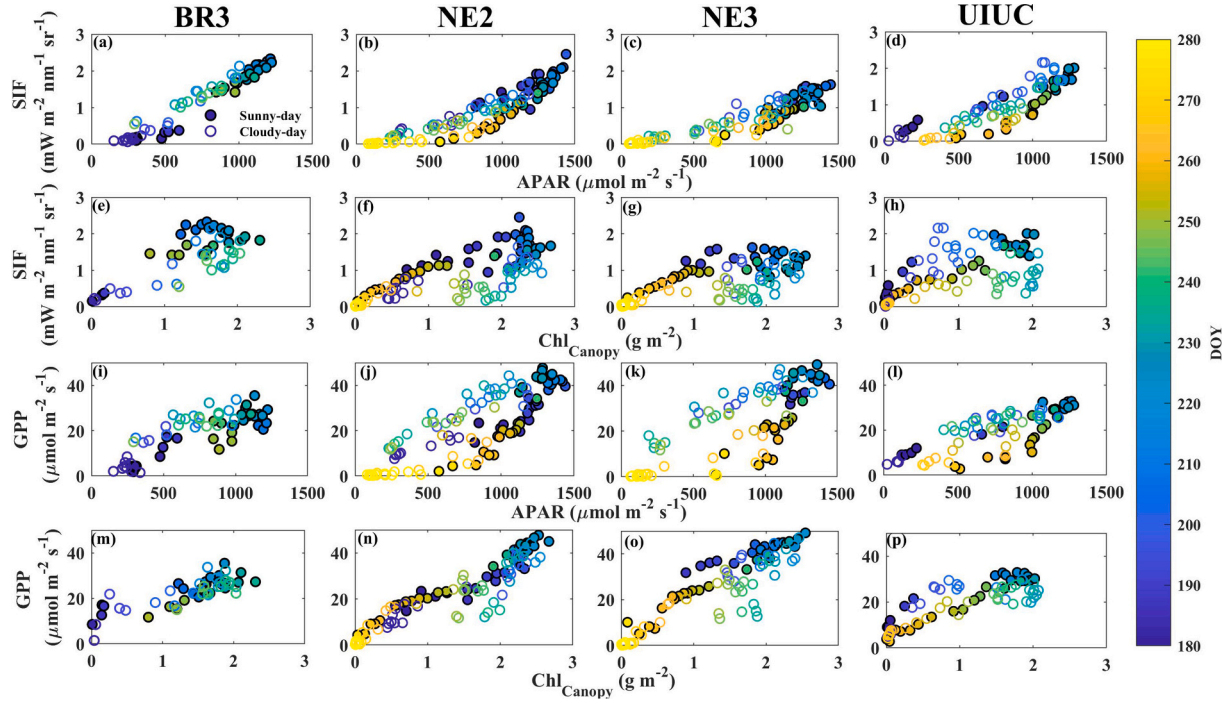

Fig. B1. Scatterplot between daytime mean APAR and SIF (a-d), between Chl_{Canopy} and SIF (e-h), between APAR and GPP (i-l), and Chl_{Canopy} and GPP (m-p) at the four soybean fields: (a, e, i, m) BR3, (b, f, j, n) NE2, (c, g, k, o) NE3 and (d, h, l, p) UIUC. Filled circles are sunny days and open circles are cloudy days. Colormap represents day of year (DOY). All data used are daytime mean values.

Appendix C. Direct comparison between SCOPE estimates and tower observations

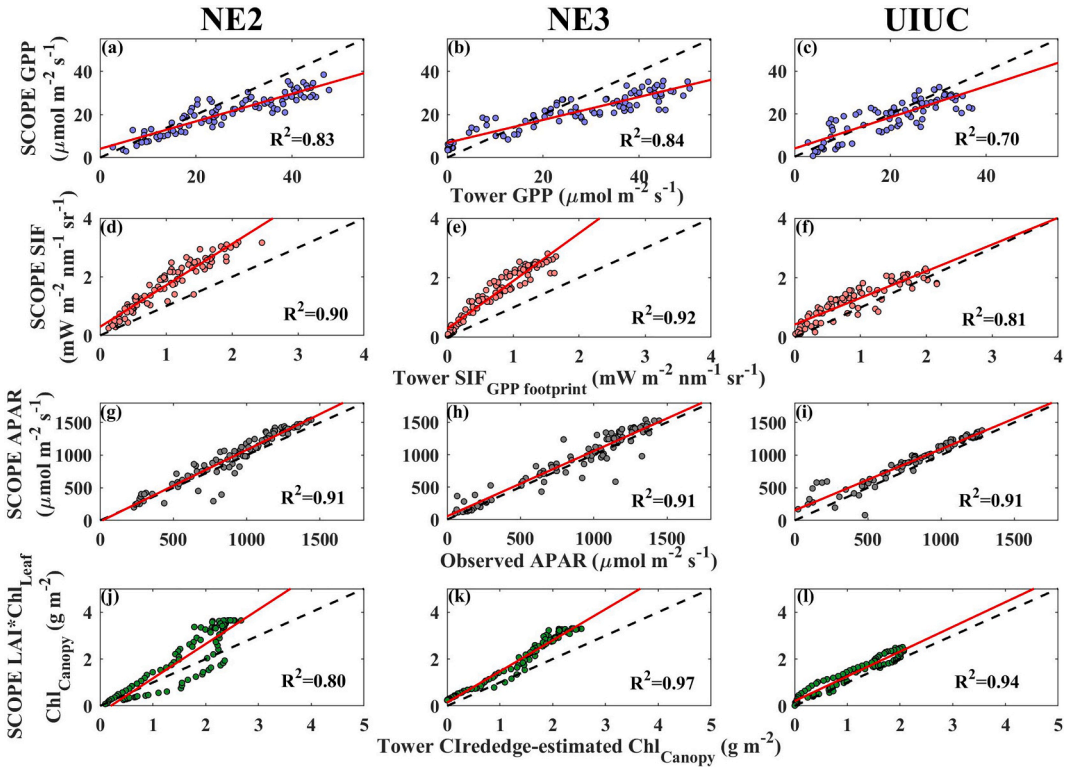

Fig. C1. Relationship between SCOPE estimated SIF, GPP, APAR, Chl_{Canopy} and tower SIF, GPP, APAR and Chl_{Canopy}. Black dashed line is 1:1 line and the red solid line is linear regression line. R^2 of the linear regression between SCOPE estimates and tower data are shown as texts.

Appendix D. The comparison between Chl_{Canopy} and the product of Chl_{Canopy} and PAR

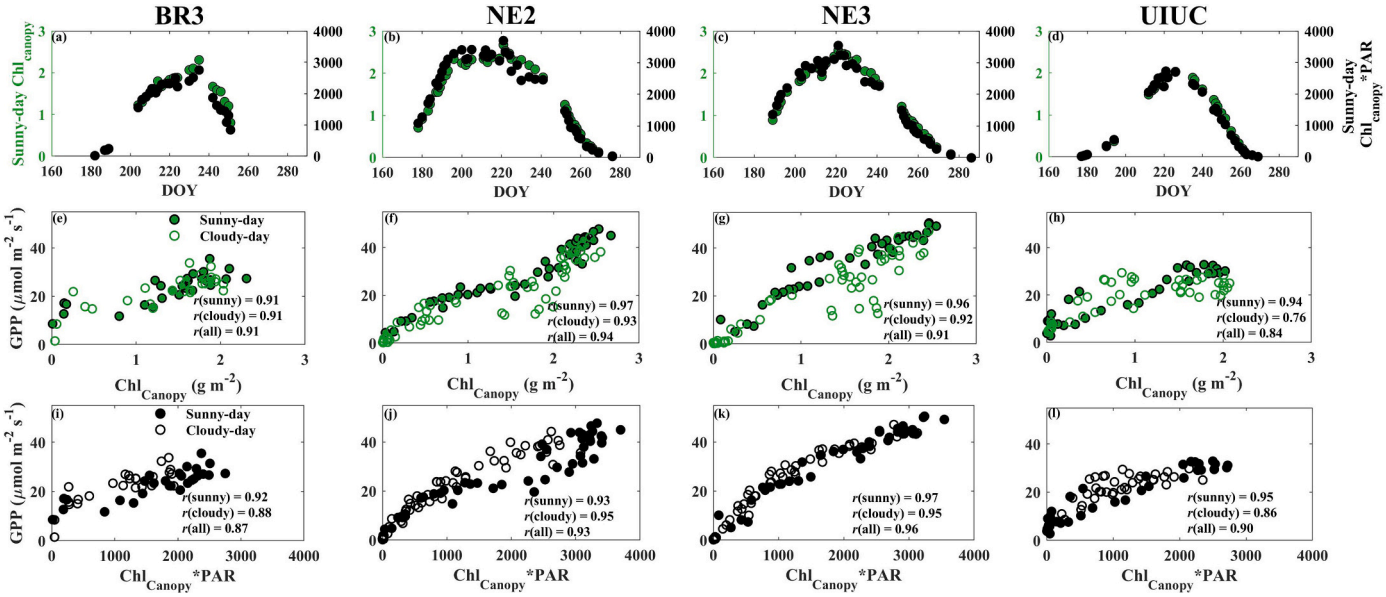

Fig. D1. The comparison between Chl_{Canopy} and the product of Chl_{Canopy} and PAR (Chl_{Canopy}*PAR), and their relationships with GPP. Seasonal variations of sunny-day Chl_{Canopy} (green circles) and Chl_{Canopy}*PAR (black circles) at the (a) BR3, (b) NE2, (c) NE3 and (d) UIUC site, the relationship between Chl_{Canopy} and GPP at the (e) BR3, (f) NE2, (g) NE3 and (h) UIUC, and the relationship between the product of Chl_{Canopy} and PAR (Chl_{Canopy}*PAR) and GPP at the (i) BR3, (j) NE2, (k) NE3 and (l) UIUC. Filled circles are sunny days and open circles are cloudy days. The Pearson correlation coefficients (r) between Chl_{Canopy} and GPP and between Chl_{Canopy}*PAR and GPP on sunny days, cloudy days and all days are shown as texts.

Appendix E. Supplementary data

Supplementary data to this article can be found online at https://doi.org/10.1016/j.rse.2022.113104.

References

Ainsworth, E.A., Yendrek, C.R., Skoneczka, J.A., Long, S.P., 2012. Accelerating yield potential in soybean: potential targets for biotechnological improvement. Plant Cell Environ. 35, 38–52. https://doi.org/10.1111/j.1365-3040.2011.02378.x.

Alonso, L., Gomez-Chova, L., Vila-Frances, J., Amoros-Lopez, J., Guanter, L., Calpe, J., Moreno, J., 2008. Improved fraunhofer line discrimination method for vegetation fluorescence quantification. IEEE Geosci. Remote Sens. Lett. 5, 620–624. https://doi.org/10.1109/LGRS.2008.2001180.

Badgley, G., Field, C.B., Berry, J.A., 2017. Canopy near-infrared reflectance and terrestrial photosynthesis. Sci. Adv. 3, 1602244. https://doi.org/10.1126/sciadv.1602244.

Beck, P.S.A., Atzberger, C., Høgda, K.A., Johansen, B., Skidmore, A.K., 2006. Improved monitoring of vegetation dynamics at very high latitudes: a new method using MODIS NDVI. Remote Sens. Environ. 100, 321–334. https://doi.org/10.1016/j.rse.2005.10.021.

Belda, S., Pipia, L., Morcillo-Pallarés, P., Rivera-Caicedo, J.P., Amin, E., De Grave, C., Verrelst, J., 2020. DATimeS: a machine learning time series GUI toolbox for gap-filling and vegetation phenology trends detection. Environ. Model. Softw. 127 https://doi.org/10.1016/j.envsoft.2020.104666.

Berger, K., Atzberger, C., Danner, M., D'Urso, G., Mauser, W., Vuolo, F., Hank, T., 2018. Evaluation of the PROSAIL model capabilities for future hyperspectral model environments: a review study. Remote Sens. 10 https://doi.org/10.3390/rs10010085.

Celesti, M., van der Tol, C., Cogliati, S., Panigada, C., Yang, P., Pinto, F., Rascher, U., Miglietta, F., Colombo, R., Rossini, M., 2018. Exploring the physiological information of Sun-induced chlorophyll fluorescence through radiative transfer model inversion. Remote Sens. Environ. 215, 97–108. https://doi.org/10.1016/j.rse.2018.05.013.

Cendrero-mateo, M.P., Wieneke, S., Damm, A., Alonso, L., Pinto, F., Moreno, J., Guanter, L., Celesti, M., Rossini, M., Sabater, N., Cogliati, S., Julitta, T., Rascher, U., Goulas, Y., 2019. Sun-Induced Chlorophyll Fluorescence III : Benchmarking Retrieval Methods and Sensor Characteristics for Proximal Sensing.

Chang, C.Y., Guanter, L., Frankenberg, C., Köhler, P., Gu, L., Magney, T.S., Grossmann, K., Sun, Y., 2020. Systematic assessment of retrieval methods for canopy far-red solar-induced chlorophyll fluorescence using high-frequency automated field spectroscopy. J. Geophys. Res. Biogeosci. 125, 1–26. https://doi.org/10.1029/2019JG005533.

Clevers, J.G.P.W., Kooistra, L., Van Den Brande, M.M.M., 2017. Using Sentinel-2 Data for Retrieving LAI and Leaf and Canopy Chlorophyll Content of a Potato Crop 1–15. https://doi.org/10.3390/rs9050405.

Croft, H., Chen, J.M., Froelich, N.J., Chen, B., Staebler, R.M., 2015. Seasonal controls of canopy chlorophyll content on forest carbon uptake: Implications for GPP modeling. J. Geophys. Res. G Biogeosciences 120, 1576–1586. https://doi.org/10.1002/2015JG002980.

Croft, H., Chen, J.M., Luo, X., Bartlett, P., Chen, B., Staebler, R.M., 2017. Leaf chlorophyll content as a proxy for leaf photosynthetic capacity. Glob. Chang. Biol. 23, 3513–3524. https://doi.org/10.1111/gcb.13599.

Damm, A., Elber, J., Erler, A., Gioli, B., Hamdi, K., Hutjes, R., Kosvancova, M., Meroni, M., Miglietta, F., Moersch, A., Moreno, J., Schickling, A., Sonnenschein, R., Udelhoven, T., van der Linden, S., Hostert, P., Rascher, U., 2010. Remote sensing of sun-induced fluorescence to improve modeling of diurnal courses of gross primary production (GPP). Glob. Chang. Biol. 16, 171–186. https://doi.org/10.1111/j.1365-2486.2009.01908.x.

Damm, A., Erler, A., Hillen, W., Meroni, M., Schaepman, M.E., Verhoef, W., Rascher, U., 2011. Modeling the impact of spectral sensor configurations on the FLD retrieval accuracy of sun-induced chlorophyll fluorescence. Remote Sens. Environ. 115, 1882–1892. https://doi.org/10.1016/j.rse.2011.03.011.

Darvishzadeh, R., Skidmore, A., Schlerf, M., Atzberger, C., 2008. Inversion of a radiative transfer model for estimating vegetation LAI and chlorophyll in a heterogeneous grassland. Remote Sens. Environ. https://doi.org/10.1016/j.rse.2007.12.003.

Dash, J., Curran, P.J., 2004. The MERIS terrestrial chlorophyll index. Int. J. Remote Sens. 25, 5403–5413. https://doi.org/10.1080/0143116042000274015.

Dechant, B., Ryu, Y., Badgley, G., Zeng, Y., Berry, J.A., Zhang, Y., Goulas, Y., Li, Z., Zhang, Q., Kang, M., Li, J., Moya, I., 2020. Canopy structure explains the relationship between photosynthesis and sun-induced chlorophyll fluorescence in crops. Remote Sens. Environ. 241 https://doi.org/10.1016/j.rse.2020.111733.

Dechant, B., Ryu, Y., Badgley, G., Köhler, P., Rascher, U., Migliavacca, M., Zhang, Y., Tagliabue, G., Guan, K., Rossini, M., Goulas, Y., Zeng, Y., Frankenberg, C., Berry, J. A., 2022. NIRVP: a robust structural proxy for sun-induced chlorophyll fluorescence and photosynthesis across scales. Remote Sens. Environ. 268 https://doi.org/10.1016/j.rse.2021.112763.

Delloye, C., Weiss, M., Defourny, P., 2018. Retrieval of the canopy chlorophyll content from Sentinel-2 spectral bands to estimate nitrogen uptake in intensive winter wheat cropping systems. Remote Sens. Environ. 216, 245–261. https://doi.org/10.1016/j.rse.2018.06.037.

Dinç, E., Ceppi, M.G., Tóth, S.Z., Bottka, S., Schansker, G., 2012. The chl a fluorescence intensity is remarkably insensitive to changes in the chlorophyll content of the leaf as long as the chl a/b ratio remains unaffected. Biochim. Biophys. Acta Bioenerg. 1817, 770–779. https://doi.org/10.1016/J.BBABIO.2012.02.003.

Dold, C., Büyükcangaz, H., Rondinelli, W., Prueger, J.H., Sauer, T.J., Hatfield, J.L., 2017. Long-term carbon uptake of agro-ecosystems in the Midwest. Agric. For. Meteorol. 232, 128–140. https://doi.org/10.1016/j.agrformet.2016.07.012.

Dold, C., Hatfield, J.L., Prueger, J.H., Moorman, T.B., Sauer, T.J., Cosh, M.H., Drewry, D. T., Wacha, K.M., 2019. Upscaling gross primary production in corn-soybean rotation systems in the Midwest. Remote Sens. 11 https://doi.org/10.3390/rs11141688.

Duveiller, G., Filipponi, F., Walther, S., Köhler, P., Frankenberg, C., Guanter, L., Cescatti, A., 2019. A spatially downscaled sun-induced fluorescence global product for enhanced monitoring of vegetation productivity. Earth Syst. Sci. Data Discuss. 1–24 https://doi.org/10.5194/essd-2019-121.

Eilers, P.H.C., 2003. A perfect smoother. Anal. Chem. 75, 3631–3636. https://doi.org/10.1021/ac034173t.

Farquhar, G.D., von Caemmerer, S., Berry, J.A., 1980. A biochemical model of photosynthetic CO2 assimilation in leaves of C3 species. Planta 149, 78–90. https://doi.org/10.1007/BF00386231.

Frankenberg, C., Berry, J., 2018. Solar Induced Chlorophyll Fluorescence: Origins, Relation to Photosynthesis and Retrieval, Comprehensive Remote Sensing. Elsevier. https://doi.org/10.1016/B978-0-12-409548-9.10632-3.

Frankenberg, C., Fisher, J.B., Worden, J., Badgley, G., Saatchi, S.S., Lee, J.E., Toon, G.C., Butz, A., Jung, M., Kuze, A., Yokota, T., 2011. New global observations of the terrestrial carbon cycle from GOSAT: patterns of plant fluorescence with gross primary productivity. Geophys. Res. Lett. 38, 1–22. https://doi.org/10.1029/2011GL048738.

Gamon, J.A., Serrano, L., Surfus, J.S., 1997. The photochemical reflectance index: an optical indicator of photosynthetic radiation use efficiency across species, functional types, and nutrient levels. Oecologia 112, 492–501. https://doi.org/10.1007/s004420050337.

Gitelson, A.A., Gamon, J.A., 2015. The need for a common basis for defining light-use efficiency: implications for productivity estimation. Remote Sens. Environ. 156, 196–201. https://doi.org/10.1016/j.rse.2014.09.017.

Gitelson, A.A., Viña, A., Ciganda, V., Rundquist, D.C., Arkebauer, T.J., 2005. Remote estimation of canopy chlorophyll content in crops. Geophys. Res. Lett. 32 https://doi.org/10.1029/2005GL022688.

Gitelson, A.A., Viña, A., Verma, S.B., Rundquist, D.C., Arkebauer, T.J., Keydan, G., Leavitt, B., Ciganda, V., Burba, G.G., Suyker, A.E., 2006. Relationship between gross primary production and chlorophyll content in crops: implications for the synoptic monitoring of vegetation productivity. J. Geophys. Res. Atmos. 111, 1–13. https://doi.org/10.1029/2005JD006017.

Gitelson, A.A., Peng, Y., Masek, J.G., Rundquist, D.C., Verma, S., Suyker, A., Baker, J.M., Hatfield, J.L., Meyers, T., 2012. Remote estimation of crop gross primary production with Landsat data. Remote Sens. Environ. 121, 404–414. https://doi.org/10.1016/j.rse.2012.02.017.

Gitelson, A.A., Peng, Y., Huemmrich, K.F., 2014. Relationship between fraction of radiation absorbed by photosynthesizing maize and soybean canopies and NDVI from remotely sensed data taken at close range and from MODIS 250m resolution data. Remote Sens. Environ. 147, 108–120. https://doi.org/10.1016/j.rse.2014.02.014.

Gitelson, A.A., Peng, Y., Arkebauer, T.J., Suyker, A.E., 2015. Productivity, absorbed photosynthetically active radiation, and light use efficiency in crops: Implications for remote sensing of crop primary production. J. Plant Physiol. 177, 100–109. https://doi.org/10.1016/j.jplph.2014.12.015.

Gitelson, A.A., Arkebauer, T.J., Suyker, A.E., 2018. Convergence of daily light use efficiency in irrigated and rainfed C3 and C4 crops. Remote Sens. Environ. 217, 30–37. https://doi.org/10.1016/j.rse.2018.08.007.

Grossmann, K., Hurlock, S.C., Seibt, U., Stutz, J., Frankenberg, C., Magney, T.S., Hurlock, S.C., Seibt, U., Stutz, J., 2018. PhotoSpec: a new instrument to measure spatially distributed red and far-red Solar-Induced Chlorophyll Fluorescence. Remote Sens. Environ. 216, 311–327. https://doi.org/10.1016/j.rse.2018.07.002.

Gu, L., Baldocchi, D., Verma, S.B., Black, T.A., Vesala, T., Falge, E.M., Dowty, P.R., 2002. Advantages of diffuse radiation for terrestrial ecosystem productivity. J. Geophys. Res. Atmos. 107 https://doi.org/10.1029/2001jd001242.

Gu, L., Han, J., Wood, J.D., Chang, C.Y.Y., Sun, Y., 2019. Sun-induced Chl fluorescence and its importance for biophysical modeling of photosynthesis based on light reactions. New Phytol. 223, 1179–1191. https://doi.org/10.1111/nph.15796.

Guan, K., Berry, J.A., Zhang, Y., Joiner, J., Guanter, L., Badgley, G., Lobell, D.B., 2016. Improving the monitoring of crop productivity using spaceborne solar-induced fluorescence. Glob. Chang. Biol. 22, 716–726. https://doi.org/10.1111/gcb.13136.

Guanter, L., Zhang, Y., Jung, M., Joiner, J., Voigt, M., Berry, J.A., Frankenberg, C., Huete, A.R., Zarco-Tejada, P., Lee, J.E.J.-E., Moran, M.S., Ponce-Campos, G., Beer, C., Camps-Valls, G., Buchmann, N., Gianelle, D., Klumpp, K., Cescatti, A., Baker, J.M., Griffis, T.J., 2014. Global and time-resolved monitoring of crop photosynthesis with chlorophyll fluorescence. Proc. Natl. Acad. Sci. 111, E1327–E1333. https://doi.org/10.1073/pnas.1320008111.

Hao, D., Zeng, Y., Zhang, Z., Zhang, Y., Qiu, H., Biriukova, K., Celesti, M., Rossini, M., Zhu, P., Asrar, G.R., Chen, M., 2022. Adjusting solar-induced fluorescence to nadir-viewing provides a better proxy for GPP. ISPRS J. Photogramm. Remote Sens. 186, 157–169. https://doi.org/10.1016/J.ISPRSJPRS.2022.01.016.

He, L., Chen, J.M., Liu, J., Mo, G., Joiner, J., 2017. Angular normalization of GOME-2 Sun-induced chlorophyll fluorescence observation as a better proxy of vegetation productivity. Geophys. Res. Lett. 44, 5691–5699. https://doi.org/10.1002/2017GL073708.

He, L., Magney, T., Dutta, D., Yin, Y., Köhler, P., Grossmann, K., Stutz, J., Dold, C., Hatfield, J., Guan, K., Peng, B., Frankenberg, C., 2020. From the ground to space: using solar-induced chlorophyll fluorescence to estimate crop productivity. Geophys. Res. Lett. 47, 1–12. https://doi.org/10.1029/2020GL087474.

Helm, L.T., Shi, H., Lerdau, M.T., Yang, X., 2020. Solar-induced chlorophyll fluorescence and short-term photosynthetic response to drought. Ecol. Appl. 30, 1–12. https://doi.org/10.1002/eap.2101.

Houborg, R., McCabe, M., Cescatti, A., Gao, F., Schull, M., Gitelson, A., 2015a. Joint leaf chlorophyll content and leaf area index retrieval from Landsat data using a regularized model inversion system (REGFLEC). Remote Sens. Environ. 159, 203–221. https://doi.org/10.1016/j.rse.2014.12.008.

Houborg, R., McCabe, M.F., Cescatti, A., Gitelson, A.A., 2015b. Leaf chlorophyll constraint on model simulated gross primary productivity in agricultural systems. Int. J. Appl. Earth Obs. Geoinf. 43, 160–176. https://doi.org/10.1016/j.jag.2015.03.016.

Huemmrich, K.F., 2013. Simulations of seasonal and latitudinal variations in leaf inclination angle distribution: implications for remote sensing. Adv. Remote Sens. 02, 93–101. https://doi.org/10.4236/ars.2013.22013.

Inoue, Y., Guérif, M., Baret, F., Skidmore, A., Gitelson, A., Schlerf, M., Darvishzadeh, R., Olioso, A., 2016. Simple and robust methods for remote sensing of canopy chlorophyll content: a comparative analysis of hyperspectral data for different types of vegetation. Plant Cell Environ. 39, 2609–2623. https://doi.org/10.1111/pce.12815.

Jiang, C., Guan, K., Wu, G., Peng, B., Wang, S., 2020. A daily, 250 m, and real-time gross primary productivity product (2000 – present) covering the Contiguous United States. Earth Syst. Sci. Data 1786.

Joiner, J., Guanter, L., Lindstrot, R., Voigt, M., Vasilkov, A.P., Middleton, E.M., Huemmrich, K.F., Yoshida, Y., Frankenberg, C., 2013. Global monitoring of terrestrial chlorophyll fluorescence from moderate-spectral-resolution near-infrared satellite measurements: methodology, simulations, and application to GOME-2. Atmos. Meas. Tech. 6, 2803–2823. https://doi.org/10.5194/amt-6-2803-2013.

Kim, J., Ryu, Y., Dechant, B., Lee, H., Kim, H.S.H.S., Kornfeld, A., Berry, J.A., 2021. Solar-induced chlorophyll fluorescence is nonlinearly related to canopy photosynthesis in a temperate evergreen needleleaf forest. Remote Sens. Environ. 112362 https://doi.org/10.1016/j.rse.2021.112362. In press.

Kimm, H., Guan, K., Jiang, C., Miao, G., Wu, G., Suyker, A.E., Ainsworth, E.A., Bernacchi, C.J., Montes, C.M., Berry, J.A., Yang, X., Frankenberg, C., Chen, M., Köhler, P., 2021. A physiological signal derived from sun-induced chlorophyll fluorescence quantifies crop physiological response to environmental stresses in the U.S. Corn Belt. Environ. Res. Lett. 16, 124051 https://doi.org/10.1088/1748-9326/ac3b16.

Kira, O., Nguy-Robertson, A.L., Arkebauer, T.J., Linker, R., Gitelson, A.A., 2017. Toward generic models for green LAI estimation in maize and soybean: satellite observations. Remote Sens. 9, 1–16. https://doi.org/10.3390/rs9040318.

Koffi, E.N., Rayner, P.J., Norton, A.J., Frankenberg, C., Scholze, M., 2015. Investigating the usefulness of satellite-derived fluorescence data in inferring gross primary productivity within the carbon cycle data assimilation system. Biogeosciences 12, 4067–4084. https://doi.org/10.5194/bg-12-4067-2015.

Köhler, P., Frankenberg, C., Landgraf, J., Magney, T.S., Guanter, L., Köehler, P., Frankenberg, C., Magney, T.S., Guanter, L., Joiner, J., Landgraf, J., Köhler, P., Frankenberg, C., Magney, T.S., Guanter, L., Joiner, J., Landgraf, J., 2018. Global Retrievals of Solar-Induced Chlorophyll Fluorescence With TROPOMI: First Results and Intersensor Comparison to OCO-2. Geophys. Res. Lett. 45, 456–463. https://doi.org/10.1029/2018GL079031.

Li, X., Xiao, J., 2019. Mapping photosynthesis solely from solar-induced chlorophyll fluorescence: a global, fine-resolution dataset of gross primary production derived from OCO-2. Remote Sens. 11 https://doi.org/10.3390/rs11212563.

Li, X., Xiao, J., He, B., Altaf Arain, M., Beringer, J., Desai, A.R., Emmel, C., Hollinger, D. Y., Krasnova, A., Mammarella, I., Noe, S.M., Ortiz, P.S., Rey-Sanchez, A.C., Rocha, A. V., Varlagin, A., Arain, M.A., Beringer, J., Desai, A.R., Emmel, C., Hollinger, D.Y., Krasnova, A., Mammarella, I., Noe, S.M., Adrian, A.C.R., Andrej, V.R., 2018. Solar-induced chlorophyll fluorescence is strongly correlated with terrestrial photosynthesis for a wide variety of biomes: first global analysis based on OCO-2 and flux tower observations. Glob. Chang. Biol. 24, 3990–4008. https://doi.org/10.1111/gcb.14297.

Li, J., Zhang, Y., Gu, L., Li, Z., Li, Jing, Zhang, Q., Zhang, Z., Song, L., 2020. Seasonal variations in the relationship between sun-induced chlorophyll fluorescence and photosynthetic capacity from the leaf to canopy level in a rice crop. J. Exp. Bot. 71, 7179–7197. https://doi.org/10.1093/jxb/eraa408.

Liu, X., Liu, L., Hu, J., Du, S., 2017. Modeling the footprint and equivalent radiance transfer path length for tower-based hemispherical observations of chlorophyll fluorescence. Sensors (Switzerland) 17, 1–15. https://doi.org/10.3390/s17051131.

Liu, L., Liu, X., Chen, J., Du, S., Ma, Y., Qian, X., Chen, S., Peng, D., 2020. Estimating maize GPP using near-infrared radiance of vegetation. Sci. Remote Sens. 2, 100009 https://doi.org/10.1016/j.srs.2020.100009.

Long, S.P., Ainsworth, E.A., Leakey, A.D.B., Ort, D.R., No, J., 2006. Food for Thought : Lower-Than, 312, pp. 1918–1922.

Lu, X., Liu, Z., Zhou, Y., Liu, Y., An, S., Tang, J., 2018. Comparison of phenology estimated from reflectance-based indices and solar-induced chlorophyll fluorescence (SIF) observations in a temperate forest using GPP-based phenology as the standard. Remote Sens. 10 https://doi.org/10.3390/rs10060932.

Lu, X., Ju, W., Li, J., Croft, H., Chen, J.M., Luo, Y., Yu, H., Hu, H., 2020. Maximum carboxylation rate estimation with chlorophyll content as a proxy of Rubisco content. J. Geophys. Res. Biogeosci. 125, 1–14. https://doi.org/10.1029/2020JG005748.

Magney, T.S., Frankenberg, C., Köhler, P., North, G., Davis, T.S., Dold, C., Dutta, D., Fisher, J.B., Grossmann, K., Harrington, A., Hatfield, J., Stutz, J., Sun, Y., Porcar-Castell, A., 2019. Disentangling changes in the spectral shape of chlorophyll fluorescence: implications for remote sensing of photosynthesis. J. Geophys. Res. Biogeosci. 124, 0–2. https://doi.org/10.1029/2019JG005029.

Magney, T.S., Barnes, M.L., Yang, X., 2020. On the covariation of chlorophyll fluorescence and photosynthesis across scales. Geophys. Res. Lett. 47, 1–7. https://doi.org/10.1029/2020GL091098.

Marrs, J.K., Reblin, J.S., Logan, B.A., Allen, D.W., Reinmann, A.B., Bombard, D.M., Tabachnik, D., Hutyra, L.R., 2020. Solar-induced fluorescence does not track photosynthetic carbon assimilation following induced stomatal closure. Geophys. Res. Lett. 47, 1–11. https://doi.org/10.1029/2020GL087956.

Marrs, J.K., Jones, T.S., Allen, D.W., Hutyra, L.R., 2021. Instrumentation sensitivities for tower-based solar-induced fluorescence measurements. Remote Sens. Environ. 259, 112413 https://doi.org/10.1016/j.rse.2021.112413.

Martini, D., Sakowska, K., Wohlfahrt, G., Pacheco-Labrador, J., van der Tol, C., Porcar-Castell, A., Magney, T.S., Carrara, A., Colombo, R., El-Madanay, T., Gonzalez-Cascon, R., Martín, M.P., Julitta, T., Moreno, G., Rascher, U., Reichstein, M., Rossini, M., Migliavacca, M., 2021. Heatwave breaks down the linearity between sun-induced fluorescence and gross primary production. New Phytol. https://doi.org/10.1111/nph.17920.

Medlyn, B.E., 1998. Physiological basis of the light use efficiency model. Tree Physiol. 18, 167–176. https://doi.org/10.1093/treephys/18.3.167.

Meroni, M., Rossini, M., Guanter, L., Alonso, L., Rascher, U., Colombo, R., Moreno, J., 2009. Remote sensing of solar-induced chlorophyll fl uorescence : Review of methods and applications, vol. 113, pp. 2037–2051. https://doi.org/10.1016/j.rse.2009.05.003.

Miao, G., Guan, K., Yang, X., Bernacchi, C.J., Berry, J.A., DeLucia, E.H., Wu, J., Moore, C. E., Meacham, K., Cai, Y., Peng, B., Kimm, H., Masters, M.D., 2018. Sun-Induced chlorophyll fluorescence, photosynthesis, and light use efficiency of a soybean field from seasonally continuous measurements. J. Geophys. Res. Biogeosci. 123, 610–623. https://doi.org/10.1002/2017JG004180.

Miao, G., Guan, K., Suyker, A.E., Yang, X., Arkebauer, T.J., Walter-Shea, E.A., Kimm, H., Hmimina, G.Y., Gamon, J.A., Franz, T.E., Frankenberg, C., Berry, J.A., Wu, G., 2020. Varying contributions of drivers to the relationship between canopy photosynthesis and far-red sun-induced fluorescence for two maize sites at different temporal scales. J. Geophys. Res. Biogeosci. 125, 1–17. https://doi.org/10.1029/2019JG005051.

Mohammed, G.H., Colombo, R., Middleton, E.M., Rascher, U., van der Tol, C., Nedbal, L., Goulas, Y., Pérez-Priego, O., Damm, A., Meroni, M., Joiner, J., Cogliati, S., Verhoef, W., Malenovský, Z., Gastellu-Etchegorry, J.P., Miller, J.R., Guanter, L., Moreno, J., Moya, I., Berry, J.A., Frankenberg, C., Zarco-Tejada, P.J., 2019. Remote sensing of solar-induced chlorophyll fluorescence (SIF) in vegetation: 50 years of progress. Remote Sens. Environ. 231, 111177 https://doi.org/10.1016/j.rse.2019.04.030.

Moncrieff, J.B., Massheder, J.M., de Bruin, H., Elbers, J., Friborg, T., Heusinkveld, B., Kabat, P., Scott, S., Soegaard, H., Verhoef, A., 1997. A system to measure surface fluxes of momentum, sensible heat, water vapour and carbon dioxide. J. Hydrol. 188–189, 589–611. https://doi.org/10.1016/S0022-1694(96)03194-0.

Moncrieff, J., Clement, R., Finnigan, J., Meyers, T., 2005. In: Lee, X., Massman, W., Law, B. (Eds.), Averaging, Detrending, and Filtering of Eddy Covariance Time Series BT - Handbook of Micrometeorology: A Guide for Surface Flux Measurement and Analysis. Springer, Netherlands, Dordrecht, pp. 7–31. https://doi.org/10.1007/1-4020-2265-4_2.

Moore, B., Crowell, S.M.R., Rayner, P.J., Kumer, J., O'Dell, C.W., O'Brien, D., Utembe, S., Polonsky, I., Schimel, D., Lemen, J., 2018. The Potential of the Geostationary Carbon Cycle Observatory (GeoCarb) to provide multi-scale constraints on the carbon cycle in the Americas. Front. Environ. Sci. 6, 1–13. https://doi.org/10.3389/fenvs.2018.00109.

Moore, C.E., von Haden, A.C., Burnham, M.B., Kantola, I.B., Gibson, C.D., Blakely, B.J., Dracup, E.C., Masters, M.D., Yang, W.H., DeLucia, E.H., Bernacchi, C.J., 2020. Ecosystem-scale biogeochemical fluxes from three bioenergy crop candidates: how energy sorghum compares to maize and miscanthus. GCB Bioenergy 13, 445–458. https://doi.org/10.1111/gcbb.12788.

Myneni, R.B., Williams, D.L., 1994. On the relationship between FAPAR and NDVI. Remote Sens. Environ. 49, 200–211. https://doi.org/10.1016/0034-4257(94)90016-7.

Nobel, P.S., Forseth, I.N., Long, S.P., 1993. Canopy structure and light interception. In: Hall, D.O., Scurlock, J.M.O., Bolhár-Nordenkampf, H.R., Leegood, R.C., Long, S.P. (Eds.), Photosynthesis and Production in a Changing Environment: A Field and Laboratory Manual. Chapman and Hall, London, pp. 79–90. https://doi.org/10.1016/b978-0-08-031999-5.50014-5.

Pacheco-Labrador, J., Perez-Priego, O., El-Madany, T.S., Julitta, T., Rossini, M., Guan, J., Moreno, G., Carvalhais, N., Martín, M.P., Gonzalez-Cascon, R., Kolle, O., Reischtein, M., van der Tol, C., Carrara, A., Martini, D., Hammer, T.W., Moossen, H., Migliavacca, M., 2019. Multiple-constraint inversion of SCOPE. Evaluating the potential of GPP and SIF for the retrieval of plant functional traits. Remote Sens. Environ. 234, 111362 https://doi.org/10.1016/j.rse.2019.111362.

Papale, D., Reichstein, M., Aubinet, M., Canfora, E., Bernhofer, C., Kutsch, W., Longdoz, B., Rambal, S., Valentini, R., Vesala, T., Yakir, D., 2006. Towards a standardized processing of Net Ecosystem Exchange measured with eddy covariance technique: algorithms and uncertainty estimation. Biogeosciences 3, 571–583. https://doi.org/10.5194/bg-3-571-2006.

Pastorello, G., Trotta, C., Canfora, E., Chu, H., Christianson, D., Cheah, Y.W., Poindexter, C., Chen, J., Elbashandy, A., Humphrey, M., Isaac, P., Polidori, D., Ribeca, A., van Ingen, C., Zhang, L., Amiro, B., Ammann, C., Arain, M.A., Ardö, J., Arkebauer, T., Arndt, S.K., Arriga, N., Aubinet, M., Aurela, M., Baldocchi, D., Barr, A., Beamesderfer, E., Marchesini, L.B., Bergeron, O., Beringer, J., Bernhofer, C., Berveiller, D., Billesbach, D., Black, T.A., Blanken, P.D., Bohrer, G., Boike, J., Bolstad, P.V., Bonal, D., Bonnefond, J.M., Bowling, D.R., Bracho, R., Brodeur, J., Brümmer, C., Buchmann, N., Burban, B., Burns, S.P., Buysse, P., Cale, P., Cavagna, M., Cellier, P., Chen, S., Chini, I., Christensen, T.R., Cleverly, J., Collalti, A., Consalvo, C., Cook, B.D., Cook, D., Coursolle, C., Cremonese, E., Curtis, P.S., D'Andrea, E., da Rocha, H., Dai, X., Davis, K.J., De Cinti, B., de Grandcourt, A., De Ligne, A., De Oliveira, R.C., Delpierre, N., Desai, A.R., Di Bella, C. M., di Tommasi, P., Dolman, H., Domingo, F., Dong, G., Dore, S., Duce, P., Dufrêne, E., Dunn, A., Dušek, J., Eamus, D., Eichelmann, U., ElKhidir, H.A.M., Eugster, W., Ewenz, C.M., Ewers, B., Famulari, D., Fares, S., Feigenwinter, I., Feitz, A., Fensholt, R., Filippa, G., Fischer, M., Frank, J., Galvagno, M., Gharun, M.,

Gianelle, D., Gielen, B., Gioli, B., Gitelson, A., Goded, I., Goeckede, M., Goldstein, A. H., Gough, C.M., Goulden, M.L., Graf, A., Griebel, A., Gruening, C., Grünwald, T., Hammerle, A., Han, S., Han, X., Hansen, B.U., Hanson, C., Hatakka, J., He, Y., Hehn, M., Heinesch, B., Hinko-Najera, N., Hörtnagl, L., Hutley, L., Ibrom, A., Ikawa, H., Jackowicz-Korczynski, M., Janouš, D., Jans, W., Jassal, R., Jiang, S., Kato, T., Khomik, M., Klatt, J., Knohl, A., Knox, S., Kobayashi, H., Koerber, G., Kolle, O., Kosugi, Y., Kotani, A., Kowalski, A., Kruijt, B., Kurbatova, J., Kutsch, W.L., Kwon, H., Launiainen, S., Laurila, T., Law, B., Leuning, R., Li, Yingnian, Liddell, M., Limousin, J.M., Lion, M., Liska, A.J., Lohila, A., López-Ballesteros, A., López-Blanco, E., Loubet, B., Loustau, D., Lucas-Moffat, A., Lüers, J., Ma, S., Macfarlane, C., Magliulo, V., Maier, R., Mammarella, I., Manca, G., Marcolla, B., Margolis, H.A., Marras, S., Massman, W., Mastepanov, M., Matamala, R., Matthes, J.H., Mazzenga, F., McCaughey, H., McHugh, I., McMillan, A.M.S., Merbold, L., Meyer, W., Meyers, T., Miller, S.D., Minerbi, S., Moderow, U., Monson, R.K., Montagnani, L., Moore, C.E., Moors, E., Moreaux, V., Moureaux, C., Munger, J.W., Nakai, T., Neirynck, J., Nesic, Z., Nicolini, G., Noormets, A., Northwood, M., Nosetto, M., Nouvellon, Y., Novick, K., Oechel, W., Olesen, J.E., Ourcival, J.M., Papuga, S.A., Parmentier, F.J., Paul-Limoges, E., Pavelka, M., Peichl, M., Pendall, E., Phillips, R.P., Pilegaard, K., Pirk, N., Posse, G., Powell, T., Prasse, H., Prober, S.M., Rambal, S., Rannik, Ü., Raz-Yaseef, N., Reed, D., de Dios, V.R., Restrepo-Coupe, N., Reverter, B.R., Roland, M., Sabbatini, S., Sachs, T., Saleska, S.R., Sánchez-Cañete, E. P., Sanchez-Mejia, Z.M., Schmid, H.P., Schmidt, M., Schneider, K., Schrader, F., Schroder, I., Scott, R.L., Sedlák, P., Serrano-Ortíz, P., Shao, C., Shi, P., Shironya, I., Siebicke, L., Šigut, L., Silberstein, R., Sirca, C., Spano, D., Steinbrecher, R., Stevens, R.M., Sturtevant, C., Suyker, A., Tagesson, T., Takanashi, S., Tang, Y., Tapper, N., Thom, J., Tiedemann, F., Tomassucci, M., Tuovinen, J.P., Urbanski, S., Valentini, R., van der Molen, M., van Gorsel, E., van Huissteden, K., Varlagin, A., Verfaillie, J., Vesala, T., Vincke, C., Vitale, D., Vygodskaya, N., Walker, J.P., Walter-Shea, E., Wang, H., Weber, R., Westermann, S., Wille, C., Wofsy, S., Wohlfahrt, G., Wolf, S., Woodgate, W., Li, Yuelin, Zampedri, R., Zhang, J., Zhou, G., Zona, D., Agarwal, D., Biraud, S., Torn, M., Papale, D., 2020. The FLUXNET2015 dataset and the ONEFlux processing pipeline for eddy covariance data. Sci. data 7, 225. https://doi.org/10.1038/s41597-020-0534-3.

Paul-Limoges, E., Damm, A., Hueni, A., Liebisch, F., Eugster, W., Schaepman, M.E., Buchmann, N., 2018. Effect of environmental conditions on sun-induced fluorescence in a mixed forest and a cropland. Remote Sens. Environ. 219, 310–323. https://doi.org/10.1016/J.RSE.2018.10.018.

Peng, Y., Gitelson, A.A., 2012. Remote estimation of gross primary productivity in soybean and maize based on total crop chlorophyll content. Remote Sens. Environ. 117, 440–448. https://doi.org/10.1016/j.rse.2011.10.021.

Peng, Y., Gitelson, A.A., Keydan, G., Rundquist, D.C., Moses, W., 2011. Remote estimation of gross primary production in maize and support for a new paradigm based on total crop chlorophyll content. Remote Sens. Environ. 115, 978–989. https://doi.org/10.1016/j.rse.2010.12.001.

Platt, U., 2017. Air monitoring by differential optical absorption spectroscopy. Encycl. Anal. Chem. 1–28 https://doi.org/10.1002/9780470027318.a0706.pub2.

Porcar-Castell, A., Tyystjärvi, E., Atherton, J., Van Der Tol, C., Flexas, J., Pfündel, E.E., Moreno, J., Frankenberg, C., Berry, J.A., 2014. Linking chlorophyll a fluorescence to photosynthesis for remote sensing applications: mechanisms and challenges. J. Exp. Bot. 65, 4065–4095. https://doi.org/10.1093/jxb/eru191.

Qian, X., Liu, L., Croft, H., Chen, J., 2021. Relationship between Leaf Maximum Carboxylation Rate and Chlorophyll Content Preserved across 13 Species. J. Geophys. Res. Biogeosci. https://doi.org/10.1029/2020jg006076 e2020JG006076.

Qiu, B., Ge, J., Guo, W., Pitman, A.J., Mu, M., 2020. Responses of Australian Dryland Vegetation to the 2019 Heat Wave at a Subdaily Scale. Geophys. Res. Lett. 47, 1–8. https://doi.org/10.1029/2019GL086569.

Reichstein, M., Falge, E., Baldocchi, D., Papale, D., Aubinet, M., Berbigier, P., Bernhofer, C., Buchmann, N., Gilmanov, T., Granier, A., Grünwald, T., Havránková, K., Ilvesniemi, H., Janous, D., Knohl, A., Laurila, T., Lohila, A., Loustau, D., Matteucci, G., Meyers, T., Miglietta, F., Ourcival, J.-M., Pumpanen, J., Rambal, S., Rotenberg, E., Sanz, M., Tenhunen, J., Seufert, G., Vaccari, F., Vesala, T., Yakir, D., Valentini, R., Division, E.S., Universita, T., Republic, C., Fermi, V.E., Tecnolo, P., 2005. On the separation of net ecosystem exchange into assimilation and ecosystem respiration: review and improved algorithm. Glob. Chang. Biol. 11, 1424–1439. https://doi.org/10.1111/j.1365-2486.2005.001002.x.

Rouse, J., Haas, R.H., Schell, J.A., Deering, D., 1973. Monitoring vegetation systems in the great plains with ERTS. In: In 3rd ERTS Symposium. NASA, pp. 309–317.

Ryu, Y., Berry, J.A., Baldocchi, D.D., 2019. What is global photosynthesis? History, uncertainties and opportunities. Remote Sens. Environ. 223, 95–114. https://doi.org/10.1016/j.rse.2019.01.016.

Song, L., Guanter, L., Guan, K., You, L., Huete, A., Ju, W., Zhang, Y., 2018. Satellite sun-induced chlorophyll fluorescence detects early response of winter wheat to heat stress in the Indian Indo-Gangetic Plains. Glob. Chang. Biol. 24, 4023–4037. https://doi.org/10.1111/gcb.14302.

Stocker, B.D., Wang, H., Smith, N.G., Harrison, S.P., Keenan, T.F., Sandoval, D., Davis, T., Prentice, I.C., 2020. P-model v1.0: An optimality-based light use efficiency model for simulating ecosystem gross primary production. Geosci. Model Dev. 13, 1545–1581. https://doi.org/10.5194/gmd-13-1545-2020.

Sun, Y., Frankenberg, C., Wood, J.D., Schimel, D.S., Jung, M., Guanter, L., Drewry, D.T., Verma, M., Porcar-Castell, A., Griffis, T.J., Gu, L., Magney, T.S., Köhler, P., Evans, B., Yuen, K., 2017. OCO-2 advances photosynthesis observation from space via solar-induced chlorophyll fluorescence. Science (80-.) 358, eaam5747. https://doi.org/10.1126/science.aam5747.

Suyker, A.E., Verma, S.B., 2012. Gross primary production and ecosystem respiration of irrigated and rainfed maize–soybean cropping systems over 8 years. Agric. For. Meteorol. 165, 12–24. https://doi.org/10.1016/j.agrformet.2012.05.021.

Tagliabue, G., Panigada, C., Dechant, B., Baret, F., Cogliati, S., Colombo, R., Migliavacca, M., Rademske, P., Schickling, A., Schüttemeyer, D., Verrelst, J., Rascher, U., Ryu, Y., Rossini, M., 2019. Exploring the spatial relationship between airborne-derived red and far-red sun-induced fluorescence and process-based GPP estimates in a forest ecosystem. Remote Sens. Environ. 231, 111272 https://doi.org/10.1016/j.rse.2019.111272.

Thenkabail, A., Lyon, P., Huete, J., Gitelson, A., 2011. Hyperspectral vegetation indices. In: Hyperspectral Remote Sensing of Vegetation, pp. 345–364. https://doi.org/10.1201/b11222-21.

Tubuxin, B., Rahimzadeh-Bajgiran, P., Ginnan, Y., Hosoi, F., Omasa, K., 2015. Estimating chlorophyll content and photochemical yield of photosystem II (ΦPSII) using solar-induced chlorophyll fluorescence measurements at different growing stages of attached leaves. J. Exp. Bot. 66, 5595. https://doi.org/10.1093/JXB/ERV272.

Upreti, D., Huang, W., Kong, W., Pascucci, S., Pignatti, S., Zhou, X., Ye, H., Casa, R., 2019. A comparison of hybrid machine learning algorithms for the retrieval of wheat biophysical variables from sentinel-2. Remote Sens. 11 https://doi.org/10.3390/rs11050481.

Urban, O., Janouš, D., Acosta, M., Czerný, R., Marková, I., Navrátil, M., Pavelka, M., Pokorný, R., Šprtová, M., Zhang, R., Špunda, V.R., Grace, J., Marek, M.V., 2007. Ecophysiological controls over the net ecosystem exchange of mountain spruce stand. Comparison of the response in direct vs. diffuse solar radiation. Glob. Chang. Biol. 13, 157–168. https://doi.org/10.1111/j.1365-2486.2006.01265.x.

Van Der Tol, C., Verhoef, W., Timmermans, J., Verhoef, A., Su, Z., Observations, E., 2009. An integrated model of soil-canopy spectral radiances, photosynthesis, fluorescence, temperature and energy balance 3109–3129.

Van Der Tol, C., Berry, J.A., Campbell, P.K.E., Rascher, U., 2014. Models of fluorescence and photosynthesis for interpreting measurements of solar-induced chlorophyll fluorescence. J. Geophys. Res. Biogeosci. 119 https://doi.org/10.1002/2014JG002713.

Van Gerpen, J., Knothe, G., 2008. In: Johnson, L.A., White, P.J., Galloway, R.B.T.-S. (Eds.), 16 - Bioenergy and Biofuels from Soybeans. AOCS Press, pp. 499–538. https://doi.org/10.1016/B978-1-893997-64-6.50019-6.

Verma, M., Schimel, D., Evans, B., Frankenberg, C., Beringer, J., Drewry, D.T., Magney, T., Marang, I., Hutley, L., Moore, C., Eldering, A., 2017. Effect of environmental conditions on the relationship between solar-induced fluorescence and gross primary productivity at an OzFlux grassland site. J. Geophys. Res. Biogeosci. 122, 716–733. https://doi.org/10.1002/2016JG003580.

Verrelst, J., Pablo, J., Van DerTol, C., Magnani, F., Mohammed, G., Moreno, J., 2015. Remote Sensing of Environment Global sensitivity analysis of the SCOPE model : what drives simulated canopy-leaving sun-induced fl uorescence ? Remote Sens. Environ. 166, 8–21. https://doi.org/10.1016/j.rse.2015.06.002.

Vickers, D., Mahrt, L., 1997. Quality control and flux sampling problems for tower and aircraft data. J. Atmos. Ocean. Technol. 14, 512–526. https://doi.org/10.1175/1520-0426(1997)014<0512:QCAFSP>2.0.CO;2.

Wang, H., Prentice, I.C., Keenan, T.F., Davis, T.W., Wright, I.J., Cornwell, W.K., Evans, B. J., Peng, C., 2017. Towards a universal model for carbon dioxide uptake by plants /704/47 /704/158/851 letter. Nat. Plants 3, 734–741. https://doi.org/10.1038/s41477-017-0006-8.

Wang, C., Guan, K., Peng, B., Chen, M., Jiang, C., Zeng, Y., Wu, G., Wang, S., Wu, J., Yang, X., Frankenberg, C., Köhler, P., Berry, J., Bernacchi, C., Zhu, K., Alden, C., Miao, G., 2020a. Satellite footprint data from OCO-2 and TROPOMI reveal significant spatio-temporal and inter-vegetation type variabilities of solar-induced fluorescence yield in the U.S. Midwest. Remote Sens. Environ. 241, 111728 https://doi.org/10.1016/J.RSE.2020.111728.

Wang, F., Chen, B., Lin, X., Zhang, H., 2020b. Solar-induced chlorophyll fluorescence as an indicator for determining the end date of the vegetation growing season. Ecol. Indic. 109, 105755 https://doi.org/10.1016/j.ecolind.2019.105755.

Wang, S., Guan, K., Wang, Z., Ainsworth, E.A., Zheng, T., Townsend, P.A., Li, K., Moller, C., Wu, G., Jiang, C., 2020c. Unique contributions of chlorophyll and nitrogen to predict crop photosynthetic capacity from leaf spectroscopy. J. Exp. Bot. 72, 341–354. https://doi.org/10.1093/jxb/eraa432.

Webb, E.K., Pearman, G.I., Leuning, R., 1980. Correction of flux measurements for density effects due to heat and water vapour transfer. Q. J. R. Meteorol. Soc. 106, 85–100. https://doi.org/10.1002/qj.49710644707.

Weiss, M., Baret, F., 2016. S2ToolBox Level 2 products: LAI, FAPAR, FCOVER. Sentin. ToolBox Level2 Prod.

Weiss, A., Norman, J.M.M., 1985. Partitioning solar radiation into direct and diffuse, visible and near-infrared components. Agric. For. Meteorol. 34, 205–213. https://doi.org/10.1016/0168-1923(85)90020-6.

Weiss, M., Baret, F., Myneni, R.B., Pragnère, A., Knyazikhin, Y., 2000. Investigation of a model inversion technique to estimate canopy biophysical variables from spectral and directional reflectance data. Agronomie 20, 3–22.

Wen, J., Köhler, P., Duveiller, G., Parazoo, N.C., Magney, T.S., Hooker, G., Yu, L., Chang, C.Y., Sun, Y., 2020. A framework for harmonizing multiple satellite instruments to generate a long-term global high spatial-resolution solar-induced chlorophyll fluorescence (SIF). Remote Sens. Environ. https://doi.org/10.1016/j.rse.2020.111644.

Wieneke, S., Burkart, A., Cendrero-Mateo, M.P.P., Julitta, T., Rossini, M., Schickling, A., Schmidt, M., Rascher, U., 2018. Linking photosynthesis and sun-induced fluorescence at sub-daily to seasonal scales. Remote Sens. Environ. 219, 247–258. https://doi.org/10.1016/j.rse.2018.10.019.

Wohlfahrt, G., Gerdel, K., Migliavacca, M., Rotenberg, E., Tatarinov, F., Müller, J., Hammerle, A., Julitta, T., Spielmann, F.M., Yakir, D., 2018. Sun-induced

fluorescence and gross primary productivity during a heat wave. Sci. Rep. 8, 1–9. https://doi.org/10.1038/s41598-018-32602-z.

Wu, C., Niu, Z., Tang, Q., Huang, W., Rivard, B., Feng, J., 2009. Remote estimation of gross primary production in wheat using chlorophyll-related vegetation indices. Agric. For. Meteorol. 149, 1015–1021. https://doi.org/10.1016/j.agrformet.2008.12.007.

Wu, C., Niu, Z., Gao, S., 2012. The potential of the satellite derived green chlorophyll index for estimating midday light use efficiency in maize, coniferous forest and grassland. Ecol. Indic. 14, 66–73. https://doi.org/10.1016/j.ecolind.2011.08.018.

Wu, G., Guan, K., Jiang, C., Peng, B., Kimm, H., Chen, M., Yang, X., Wang, S., Sukyer, A. E., Bernacchi, C., Moore, C.E., Zeng, Y., Berry, J., Cendrero-Mateo, M.P., 2019. Radiance-based NIR_V as a proxy for GPP of corn and soybean. Environ. Res. Lett. https://doi.org/10.1088/1748-9326/ab65cc.

Wu, G., Guan, K., Jiang, C., Peng, B., Kimm, H., Chen, M., Yang, X., Wang, S., Suyker, A. E., Bernacchi, C.J., Moore, C.E., Zeng, Y., Berry, J.A., Cendrero-Mateo, M.P., 2020. Radiance-based NIRv as a proxy for GPP of corn and soybean. Environ. Res. Lett. 15 https://doi.org/10.1088/1748-9326/ab65cc.

Yang, P., van der Tol, C., 2018. Linking canopy scattering of far-red sun-induced chlorophyll fluorescence with reflectance. Remote Sens. Environ. 209, 456–467. https://doi.org/10.1016/j.rse.2018.02.029.

Yang, K., Ryu, Y., Dechant, B., Berry, J.A., Hwang, Y., Jiang, C., Kang, M., Kim, J., Kimm, H., Kornfeld, A., Yang, X., 2018a. Sun-induced chlorophyll fluorescence is more strongly related to absorbed light than to photosynthesis at half-hourly resolution in a rice paddy. Remote Sens. Environ. 216, 658–673. https://doi.org/10.1016/j.rse.2018.07.008.

Yang, X., Shi, H., Stovall, A., Guan, K., Miao, G., Zhang, Yongguang, Zhang, Yao, Xiao, X., Ryu, Y., Lee, J.E., 2018b. FluoSpec 2—an automated field spectroscopy system to monitor canopy solar-induced fluorescence. Sensors (Switzerland) 18. https://doi.org/10.3390/s18072063.

Yang, P., Prikaziuk, E., Verhoef, W., van der Tol, C., 2020. SCOPE 2.0: A model to simulate vegetated land surface fluxes and satellite signals. Geosci. Model Dev. Discuss. 1–26. https://doi.org/10.5194/gmd-2020-251.

Yang, P., van der Tol, C., Campbell, P.K.E., Middleton, E.M., 2021. Unraveling the physical and physiological basis for the solar- induced chlorophyll fluorescence and photosynthesis relationship using continuous leaf and canopy measurements of a corn crop. Biogeosciences 18, 441–465.

Yin, Y., Byrne, B., Liu, J., Wennberg, P.O., Davis, K.J., Magney, T., Köhler, P., He, L., Jeyaram, R., Humphrey, V., Gerken, T., Feng, S., Digangi, J.P., Frankenberg, C., 2020. Cropland carbon uptake delayed and reduced by 2019 Midwest floods. AGU Adv. 1, 1–15. https://doi.org/10.1029/2019av000140.

Zeng, Y., Badgley, G., Dechant, B., Ryu, Y.Y., Chen, M., Berry, J.A.J.A.A., 2019. A practical approach for estimating the escape ratio of near-infrared solar-induced chlorophyll fluorescence. Remote Sens. Environ. 232, 111209 https://doi.org/10.1016/j.rse.2019.05.028.

Zhang, Q., Xiao, X., Braswell, B., Linder, E., Baret, F., Moore, B., 2005. Estimating light absorption by chlorophyll, leaf and canopy in a deciduous broadleaf forest using MODIS data and a radiative transfer model. Remote Sens. Environ. 99, 357–371. https://doi.org/10.1016/j.rse.2005.09.009.

Zhang, Y., Guanter, L., Berry, J.A., Joiner, J., Tol, C., Huete, A., Gitelson, A., Voigt, M., Köhler, P., van der Tol, C., Huete, A., Gitelson, A., Voigt, M., Köhler, P., 2014. Estimation of vegetation photosynthetic capacity from space-based measurements of chlorophyll fluorescence for terrestrial biosphere models. Glob. Chang. Biol. 20, 3727–3742. https://doi.org/10.1111/gcb.12664.

Zhang, Y., Guanter, L., Berry, J.A., van der Tol, C., Yang, X., Tang, J., Zhang, F., 2016. Model-based analysis of the relationship between sun-induced chlorophyll fluorescence and gross primary production for remote sensing applications. Remote Sens. Environ. 187, 145–155. https://doi.org/10.1016/j.rse.2016.10.016.

Zhang, Z., Chen, J.M., Guanter, L., He, L., Zhang, Y., 2019. From canopy-leaving to total canopy far-red fluorescence emission for remote sensing of photosynthesis: first results From TROPOMI. Geophys. Res. Lett. 46, 12030–12040. https://doi.org/10.1029/2019GL084832.

Zhang, X., Wang, J., Henebry, G.M., Gao, F., 2020a. Development and evaluation of a new algorithm for detecting 30 m land surface phenology from VIIRS and HLS time series. ISPRS J. Photogramm. Remote Sens. 161, 37–51. https://doi.org/10.1016/j.isprsjprs.2020.01.012.

Zhang, Z., Zhang, Y., Porcar-Castell, A., Joiner, J., Guanter, L., Yang, X., Migliavacca, M., Ju, W., Sun, Z., Chen, S., Martini, D., Zhang, Q., Li, Z., Cleverly, J., Wang, H., Goulas, Y., 2020b. Reduction of structural impacts and distinction of photosynthetic pathways in a global estimation of GPP from space-borne solar-induced chlorophyll fluorescence. Remote Sens. Environ. 240, 111722 https://doi.org/10.1016/j.rse.2020.111722.

Zhang, Y.Y., Zhang, Q., Liu, L., Zhang, Y.Y., Wang, S.S., Ju, W., Zhou, G., Zhou, L., Tang, J., Zhu, X., Wang, F., Huang, Y., Zhang, Z., Qiu, B., Zhang, X., Wang, S.S., Huang, C., Tang, X., Zhang, J., 2021. ChinaSpec: a network for long-term ground-based measurements of solar-induced fluorescence in China. J. Geophys. Res. Biogeosci. 126 https://doi.org/10.1029/2020JG006042.

Zoogman, P., Liu, X., Suleiman, R.M., Pennington, W.F., Flittner, D.E., Al-Saadi, J.A., Hilton, B.B., Nicks, D.K., Newchurch, M.J., Carr, J.L., Janz, S.J., Andraschko, M.R., Arola, A., Baker, B.D., Canova, B.P., Chan Miller, C., Cohen, R.C., Davis, J.E., Dussault, M.E., Edwards, D.P., Fishman, J., Ghulam, A., González Abad, G., Grutter, M., Herman, J.R., Houck, J., Jacob, D.J., Joiner, J., Kerridge, B.J., Kim, J., Krotkov, N.A., Lamsal, L., Li, C., Lindfors, A., Martin, R.V., McElroy, C.T., McLinden, C., Natraj, V., Neil, D.O., Nowlan, C.R., O'Sullivan, E.J., Palmer, P.I., Pierce, R.B., Pippin, M.R., Saiz-Lopez, A., Spurr, R.J.D., Szykman, J.J., Torres, O., Veefkind, J.P., Veihelmann, B., Wang, H., Wang, J., Chance, K., 2017. Tropospheric emissions: Monitoring of pollution (TEMPO). J. Quant. Spectrosc. Radiat. Transf. 186, 17–39. https://doi.org/10.1016/j.jqsrt.2016.05.008.